GROWTH OF SEMICONDUCTOR THIN FILMS BY PULSED LASER DEPOSITION

A DISSERTATION IN
Physics
and
Chemistry

Presented to the Faculty of the University
of Missouri-Kansas City in partial fulfillment of
the requirements for the degree

DOCTOR OF PHILOSOPHY

By
YILU LI
B.S. Changchun University of Science and Technology, CHINA 2010,
M.S. Physics, University of Missouri-Kansas City, USA 2013

Kansas City, Missouri
2016

GROWTH OF SEMICONDUCTOR THIN FILMS BY PULSED LASER DEPOSITION

Yilu Li, Candidate for the Doctor of Philosophy Degree

University of Missouri-Kansas City, 2016

ABSTRACT

Pulsed ultraviolet light from a XeF excimer laser was used to grow thin films of zinc oxide and tin dioxide on (111) p-type silicon wafers within a versatile high vacuum laser deposition system. This pulsed laser deposition system was self-designed and self-built. Parameters such as pressure, target temperature, and distance from the target to the substrate can be adjusted in the system. Scanning electron microscopy, energy dispersive X-ray spectroscopy, X-ray diffraction spectroscopy, Raman spectroscopy and ellipsometry were used to analyze the structures and properties of ZnO and SnO_2 thin films. The critical temperature required to fabricate a crystalline ZnO thin film by pulsed laser deposition was found and has been confirmed. For the SnO_2 thin film, the critical temperature required to generate a crystalline structure could not be found because of the temperature limit of the substrate heater used in the experiment. In SnO_2 thin films, thermal annealing has been used to convert into crystalline structure with (110), (101) and (211) orientations. After fabricating the amorphous SnO_2 thin films, they were put into an oven with specific temperatures to anneal them. The minimum annealing temperature range was found for converting the amorphous SnO_2 thin films into SnO_2 thin films with a crystalline structure. Thermal annealing has also been applied to some amorphous

ZnO thin films which were fabricated under the critical temperature required to produce crystalline ZnO thin films. The minimum annealing temperature range for amorphous ZnO thin films was found and only one orientation (002) shown after annealing. Laser annealing technology has also been applied for converting both amorphous ZnO and SnO_2 thin films, and results show that this method was not well suited for this attempt.

ZnO thin films and SnO_2 thin films with a crystalline structure have inportant widely used in industry, for example, application in devices such as solar cells and UV or blue-light-emitting devices. The aim of this research is to help improving the manufacturing process of ZnO and SnO_2 thin films.

Key words: pulsed laser deposition, annealing, thin films, ZnO, SnO_2

APPROVAL

The faculty listed below, appointed by the Dean of the School of Graduate Studies have examined a dissertation titled “Growth of Semiconductor Thin Films By Pulsed Laser Deposition”, presented by Yilu Li, candidate for the Doctor of Philosophy degree, and certify that in their opinion it is worthy of acceptance.

Supervisory Committee

Jerzy M. Wrobel, Ph.D. Committee Chair
Department of Physics

Michael Kruger, Ph.D.
Department of Physics

Daming Zhu, Ph.D.
Department of Physics

Zhonghua Peng, Ph.D.
Department of Chemistry

James B. Murowchick, Ph.D.
Department of Geosciences

CONTENTS

ILLUSTRATIONS

TABLES

ACKNOWLEDGEMENTS

I would like to express my sincere thanks to all who lent me a hand in my academic achievements. First of all, I would like to take this opportunity to show my sincere gratitude to my supervisor Dr. Jerzy M. Wrobel, my mentor and advisor, for his support and guidance throughout my PhD program in physics. I am very grateful to Prof. David Wieliczka, Prof. James B. Murowchick and Mr. Reid Brenner for their help with the instrumentation. I also want to express my special thanks to Prof. Michael Kruger for a lot of good advice and precious research experiences during my entire association with UMKC. Moreover, I would like to thank all committee members for making time for me out of their busy schedule and also Miss. Gabrielle Lambton for her help of editing. Finally, I appreciate my family members and friends for all their encouragement and support.

Financial support for my studies and research from the UMKC Department of Physics and Astronomy are gratefully acknowledged.

CHAPTER 1

INTRODUCTION

Thin film technology requires the development of efficient methods for the fabrication of a specific arrangement of atom layers from source materials. In order to grow thin films from a gaseous phase, it is required to first vaporize the material and incorporate atomic vapors into layers deposited on a substrate.[1-3] Thin films, fabricated through different technological approaches (e.g., physical vapor deposition (PVD), chemical vapor deposition (CVD), plasma enhanced chemical vapor deposition (PECVD), sputter deposition, liquid phase deposition), attract attention as a framework for optoelectronics, sensors, solar cells, and displays. [2-7]

1.1 Thin films

A thin film is a layer of material ranging from nanometers to several microns in thickness. The idea was introduced in the 1850s by M. Faraday; however, the industry did not pay much attention to thin films until the 1930s. At this time, the industry became interested in thin film coatings for optical, electronical and mechanical applications.[8,9] Currently, thin films are widely used in micro-electronics, semiconductor and superconductor technology, optical applications and bioceramic materials.[8] The discovery of how thin film coatings effect both the physical and chemical properties of surfaces has significantly helped to advance many areas of science and technology. The properties of a material can be improved by growing the

material in a thin film form rather than in bulk. Thin film structures can also be used to adjust properties of the materials. For example, the periodic structure of alternating thin films of different materials collectively forms a structure called a superlattice, which exploits the phenomena associated with quantum confinement restricting electronic phenomena to two-dimensions.[8] The hybrid structures of nanoparticles and organic thin films can also be used to manipulate material properties.

1.2 Thin film deposition

As thin films become more and more attractive for industry, a lot of fabrication methods have been developed. The process of fabricating a thin film on a substrate surface or on previously deposited layers is referred to as thin film deposition. A number of thin film deposition techniques have been developed.[8] Thin film deposition techniques are divided into two main categories: chemical or physical. Chemical solution deposition, chemical vapor deposition, plasma enhanced chemical vapor deposition, metal organic chemical vapor deposition and atomic layer deposition are examples of chemical processes. Thermal evaporation deposition, molecular beam epitaxy and sputtering deposition are examples of physical processes. A brief explanation of the most popular chemical and physical thin film deposition methods is given below.

Chemical solution deposition uses a liquid precursor, usually a solution of organometallic powders dissolved in an organic solvent. This is a relatively

inexpensive and simple method of growing thin films. This technique is also known as the sol-gel method.[3, 10] Chemical vapor deposition is a process where one or more volatile gas-phase precursors are transported via the vapor phase to the reaction chamber. These precursors are then deposited on a heated substrate and decompose leaving a thin film of the desired material. Chemical vapor deposition processes are used for depositing thin films of semiconductor material, conductive interconnects, and insulating dielectrics.[11] Plasma enhanced chemical vapor deposition is a type of chemical vapor deposition that occurs in a lower pressure and lower temperature environment. During this process, the material is transported in a gaseous carrier, which decomposes on the substrate surface and deposits a thin solid state layer on a substrate. Chemical reactions are involved in the process and occur after creation of a plasma (generated by two electrodes) of the reacting gases.[11] Metal organic chemical vapor deposition is a chemical deposition method used to produce epitaxial or polycrystalline thin films. It is a highly complex process and can be used for growing crystalline layers to create complex semiconductor multilayer structures. The process takes place in a gas phase at moderate pressures (10 to 760 Torr) and it has become a common process in the manufacturing of optoelectronics.[12] Atomic layer deposition is a chemical deposition process based on the sequential use of the gas phase at low temperatures. The majority of atomic layer deposition reactions use two precursors. The process is split up into two half reactions, run in sequence and repeated for each

atomic layer of reactants, which react chemically on the substrate forming the desired film.[13]

Thermal evaporation deposition uses an electric heater to melt a material and raise its vapor pressure to an appropriate range. This is done in a vacuum environment, to allow the vapor to reach the substrate without reacting with or being scattered by other gas-phase atoms in the chamber, and to reduce the incorporation of impurities from the residual gas in the vacuum chamber.[14] Molecular beam epitaxy is a particularly sophisticated form of thermal evaporation. It takes place in high vacuum or ultra-high vacuum environment. The most important aspect of evaporation deposition is the deposition rate (typically less than 3000 nm per hour) which allows the films to grow epitaxially. Deposition rates of this magnitude require a higher quality vacuum to achieve the same impurity levels as other deposition techniques. The absence of carrier gases as well as the ultra-high vacuum environment results in the highest achievable purity of the grown films.[15] Sputter deposition is a process that uses ionized noble gases to knock off atoms from the source material which then is deposited on the film substrate. During this process, the source can be kept at a relatively low temperature because this process does not require evaporation. Sputtering deposition is one of the most flexible deposition techniques. This technique is especially useful for compounds or mixtures where there are different components, which tend to evaporate at different rates.[16]

1.3 Pulsed laser deposition

For several decades, pulsed laser deposition (PLD) is one of many physical techniques used to grow thin films. The use of a pulsed laser as an energy source for evaporative film growth has been explored since the discovery of lasers in the 1960s. Significant increase of interest in this method occurred in the late 1980s after the discovery of high Tc superconductors. Growth of $YBa_2Cu_3O_7$ thin films using PLD was first reported in 1987.[8] In the 1990s and 2000s, numerous device applications based on PLD films of functional materials were explored.[8] Currently, PLD is used in thin film deposition of insulators, semiconductors, metals, high Tc superconductors, and polymers.[17-19] Biological materials such as simple protein films have also been obtained by PLD.[20-22]

Pulsed laser deposition, which is one of the physical vapor deposition methods, is becoming a popular way to more efficiently fabricate thin films. This way of fabricating the growth of thin films can be easily adapted for different applications, which is critical for creating a technological framework for industrial manufacturing. In this respect, PLD of thin films presents a promising technological approach to fabricating thin films.[8]

The interest of industrial manufacturing requires more efficient and versatile methods of thin film fabrication. PLD makes it possible to tune growth parameters and characteristics of thin films (deposition rate, film thickness and morphology) by adjusting beam parameters such as radiation wavelength, fluence, and pulse duration.

The process can be carried out in different environments including vacuum or low-pressure gaseous atmosphere. Furthermore, this technique is also considered to be a clean process meaning that compared to other techniques the chance of contamination is low.[8]

Laser ablation of the source material constitutes the basis in PLD technology. Laser ablation uses the laser radiation energy to eject surface atoms of the target and to form a plasma plume of the processed material. During the quenching of the plume a desired film is formed on the substrate surface. By creating appropriate chemical environments, it is also possible to create a chemical reaction in the laser ablation process. Typically, PLD utilizes a high-power pulsed laser beam that is focused onto a target material. The processing chamber is kept under vacuum or various low-pressure gaseous environments during the process. The laser beam ejects target atoms in a process called ablation. In result of energy absorption from the beam, the atoms in the target are excited into high-energy states that creates a plasma plume.[8] When the plasma reaches the target surface it condenses as a result of energy loss and a thin film is formed on the substrate.[8, 23, 24-28] During PLD, many processing parameters can be changed which will have a strong influence on the properties of the film. First, the laser parameters such as laser fluence, wavelength, pulse duration and repetition rate can be altered. Second, the preparation conditions, including target-to-substrate distance, substrate temperature, background gas and pressure, may be varied, all of which can influence the film growth conditions. The advantages of PLD include a

wide range of gas pressure, easy control of growth rate, clean process and a high quality of product.[8] The disadvantages of the method include possible defects in the product caused by sputtering of atoms from the surface, unsuitability for growth of large area films, and high cost of production on industrial scale.[8]

Laser ablation is the fundamental process within PLD technology. It is a process that uses a laser beam to remove material from a solid surface as illustrated in Figure 1.[26] A high intensity laser pulse of radiation incident on a solid target results in

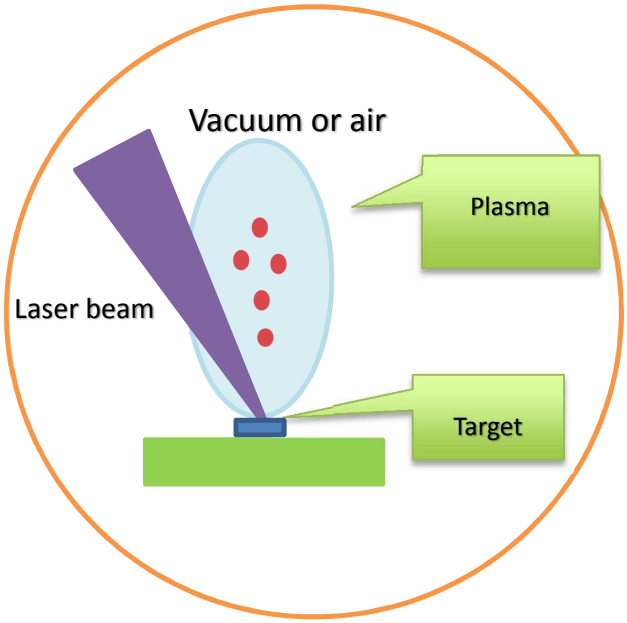

Figure 1. Schematic diagram of laser ablation

a rapid increase of surface temperature, bringing the melted layer into a metastable state.[29] When the surface temperature of the sample approaches the spinodal, homogeneous nucleation of the overheated liquid takes place causing nano-scale bubbles to form pushing the melted material and vapor outwards. This causes phase explosion and the formation of a plasma plume consisting of liquid nanodroplets, vapor and ions. This laser-induced expansion of plasma is a free expansion because this process occurs in a vacuum or a low-pressure gas environment. The ejected material expands outward from the target surface. As shown in Figure 2, some of the material is sputtered back from the substrate surface and forms a collision region

where it interacts with the incident plasma. A film grows immediately after this collision region is formed. This region serves as a source for particle condensation. When the condensation rate is higher than the rate of particles supplied by the sputtering, a film grows on the substrate surface at the expense of the direct flow of the ablated particles.[8, 30]

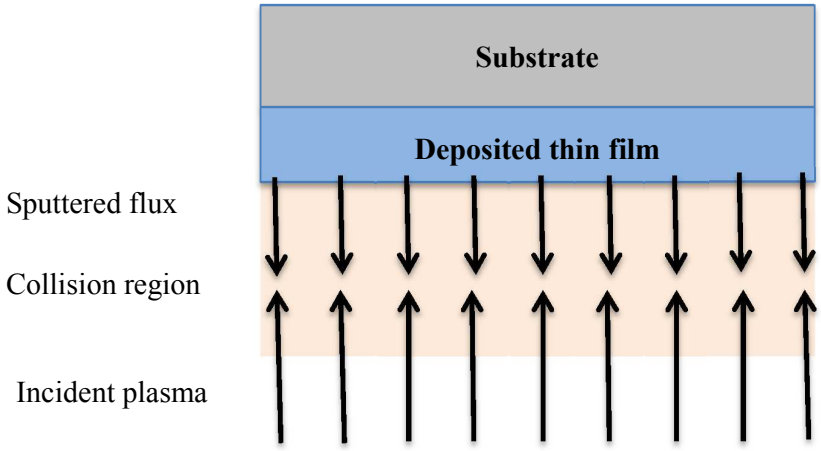

Figure 2. Schematic diagram of plasma-substrate interaction

1.4 Annealing

Annealing is a method of heating a sample to change the microstructure of the material. There is an effect on some of the physical properties of the material such as the hardness, strength or even the optical properties. For example, the hardness and structure of physical vapor deposition-based AIN(Er) films were affected by thermal annealing.[31] It has been previously reported that photonic device performance of SiO_2 waveguides was enhanced using thermal annealing of plasma enhanced chemical

vapor deposition.[32] This process has extended beyond the academic community and is now widely used in industry for the purposes of steel manufacturing.[32, 33] The thermal annealing method is performed by heating a material above its recrystallization temperature. This temperature must then be retained for a certain period of time. The final step of thermal annealing is to slowly cool the material to room temperature. During the annealing process, thermal energy is transferred to the material causing redistributions within it to produce a crystalline structure. Laser annealing is a similar technique that works by locally heating material exposed to laser radiation in order to create crystalline material. This process only works when the frequency of incident radiation is strongly absorbed by the material. Energy transferred from the laser beam causes heating on the surface which can be distributed to underlying atoms within the material. This result of this process depends on the initial material deposited on the surface: if the substance is originally crystalline, then laser annealing can reorient it into a new crystal lattice. If the starting material is amorphous, this technique can produce crystalline structures. What makes laser annealing such an interesting technique is its applicability in industry, such as the fabrication of high-efficiency solar cells.[32, 34-36]

1.5 Materials

Zinc oxide (ZnO) and tin dioxide (SnO_2) are selected for this project. These two semiconductors are widely applied on an industrial scale because of their excellent optical and electrical properties. Both materials are transparent in the visible spectral range.[23, 37] ZnO and SnO_2 are used in photoelectronic devices, as electrodes and anti-reflection coating. They are also used as catalysts, energy-saving coatings and anti-static coatings.

1.5.1 ZnO

Zinc oxide is a II-VI semiconductor, which is very stable at high temperatures and much more resistant to radiation damage than other common semiconductors. There are two main crystal structures of ZnO: hexagonal wurtzite shown in Figure 3(a) and cubic zinc blende shown in Figure 3(b).[38] In ambient conditions, the wurtzite structure is thermodynamically stable. The less stable zinc blende structure can be stabilized by growing ZnO thin film on substrates with a cubic lattice.[8, 10, 23, 38]

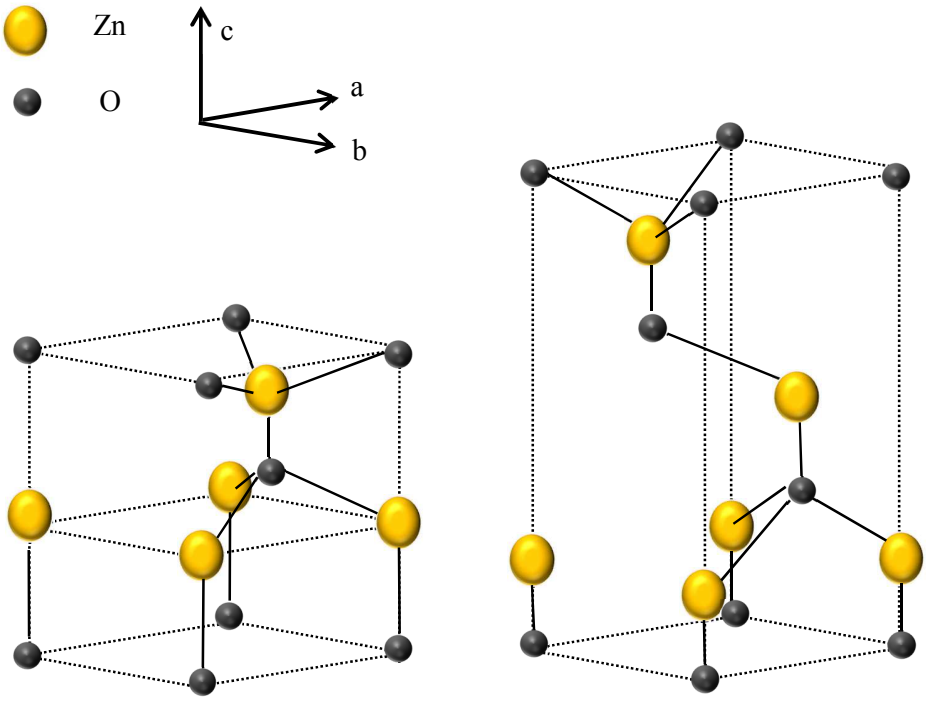

(a) hexagonal wurtzite (b) zinc blende

Figure 3. Crystal structures of ZnO

Since the bandgap energy of ZnO is 3.37eV (at room temperature), the material is transparent in both the visible and near ultraviolet wavelength regions.[38, 39] Due to its wide and direct bandgap and its large photoresponse, ZnO is also very suitable for UV photodetector applications. The 60 meV exciton binding energy in ZnO results in luminesce within the ultraviolet region (around 380 nm) and makes ZnO a possible contender for UV and blue-light-emitting devices. This large exciton binding energy permits excitonic recombination above room temperature and optically pumped lasing has been observed in epitaxial or polycrystalline ZnO thin films.[23]

1.5.2 SnO_2 thin film

Tin dioxide is usually regarded as an oxygen-deficient n-type semiconductor with the rutile structure shown in Figure 4.[19] Since the bandgap of SnO_2 is 3.7eV at room temperature, the material is also transparent in the visible light and near ultraviolet region. With the high exciton binding energy (130 meV), SnO_2 is considered to be another promising material for UV light emitting sources. It is also

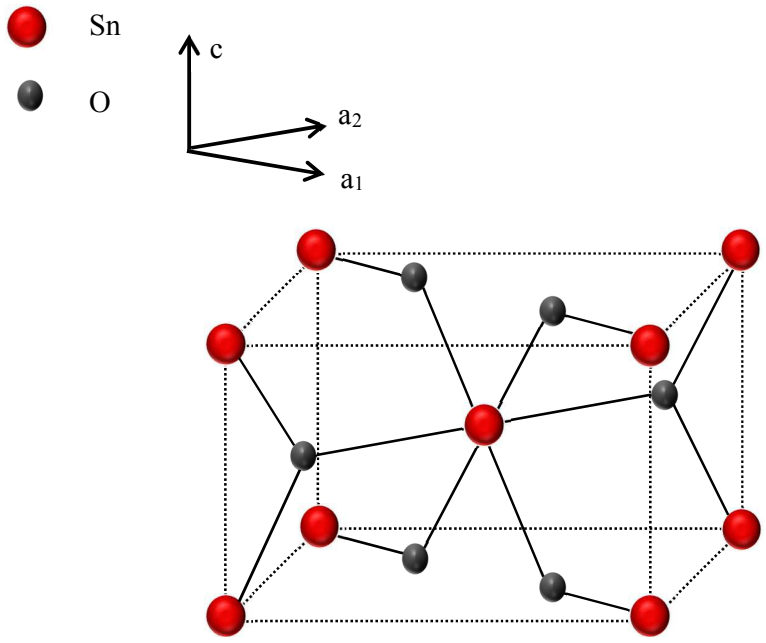

Figure 4. Rutile structure of SnO_2

an attractive semiconducting material for other optoelectronic devices because it possesses high photostability and good carrier mobility. Due to its excellent chemical and physical properties, this material is nowadays considered one of the most promising materials for producing numerous novel functional structures.[40, 41] Reduction in device size and an associated increase in the response speed can be

achieved with the advent of advanced thin film technology. Devices can be made more cost-effective and reproducible by using SnO_2 thin films.[40]

1.6 Theoretical Background of Experimental Procedures

Since pulsed laser ablation technology is based on the laser ablation process, the selection of the laser is an important aspect for the construction of laser ablation systems. Usually a shorter wavelength laser can provide a higher energy laser beam, so the UV laser is preferred as the first choice. The absorption of UV radiation in materials is usually higher compared to longer wavelengths. For this program, an excimer laser has been selected for the pulsed laser deposition.

The physical properties of the thin films were probed using several techniques. Scanning electron microscopy (SEM) was used to observe the physical morphology of the films. The characteristic X-rays produced by the electron beam produces a unique spectrum constituting the basis of energy-dispersive X-ray spectroscopy (EDS). Elemental analysis and chemical characterization of the studied materials was done using Raman spectroscopy. Ellipsometry is an optical technique which was used to measure the thickness and index of refraction of the films. Optical (UV-Vis) spectroscopy was used to measure the absorption spectra from which the bandgap energy of the film materials was determined.[39, 42] The patterns formed in X-ray diffraction (XRD) led to the identification of the film crystallinity.

1.6.1 Excimer laser

Excimer lasers are a type of pulsed gas laser, with wavelengths in the ultraviolet region. The first excimer laser was invented in 1970 by N. Basov, V. A. Danilychev and Yu. M. Popov in Moscow.[43] They used a strong electron beam to excite liquid xenon dimers, which then underwent stimulated emission at 172 nm.[43] As a gas laser, the working gas for an excimer laser consists of inert gas atoms (e.g. Ne, He, Ar, Kr, Xe) and halogen atoms (F, Cl, Br, etc.).[44] Although noble gas atoms can react with halogen atoms, the formed molecules are unstable and exist in only in the excited electronic state, which is shown schematically in Figure 5.

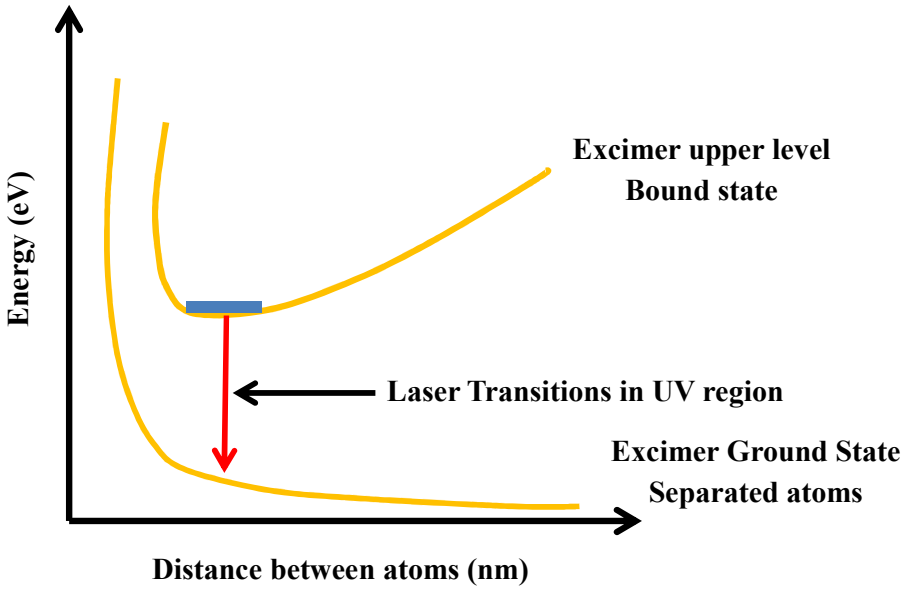

Figure 5. Energy diagram for a noble gas-halogen gas molecule (dimer). A molecule will remain in the excimer upper level for a short time before releasing a photon and returning to the ground state.

When an excited molecule releases a photon, it makes a transition from the upper level bound state to the ground state, it quickly (10^{-13} s) dissociates into two unbound atoms. Because of the very short period of such molecules in the excited state, it was named "excimer" from the phrase "excited dimer".[44] Excimer lasers, which can produce high intensity pulsed radiation, are used in many fields such as medicine, scientific research and industrial applications.[45-48]

1.6.2 Scanning electron microscopy

The first scanning electron microscope was built by V. Zworykin in 1942.[49] A scanning electron microscope takes advantage of the wave nature of electrons to image structures on the nanometer to micrometer scale.[49,50] An accelerated electron beam generated by electron gun, passes through pairs of scanning coils or pairs of deflector plates in the electron column. During the interaction with the sample, the electrons lose energy by repeated random scattering and absorption.[50] The energy exchange between the electron beam and the sample results in two different electron image signals: elastically backscattered electrons and emission of secondary electrons resulting from inelastic scattering. Each beam can be recorded by specialized detectors. The secondary electron emission, confined to a very small volume near the beam impact area can produce very high-resolution images of the sample surface. The elastically backscattered electrons can provide information about the distribution of different elements in the sample material.[49, 50]

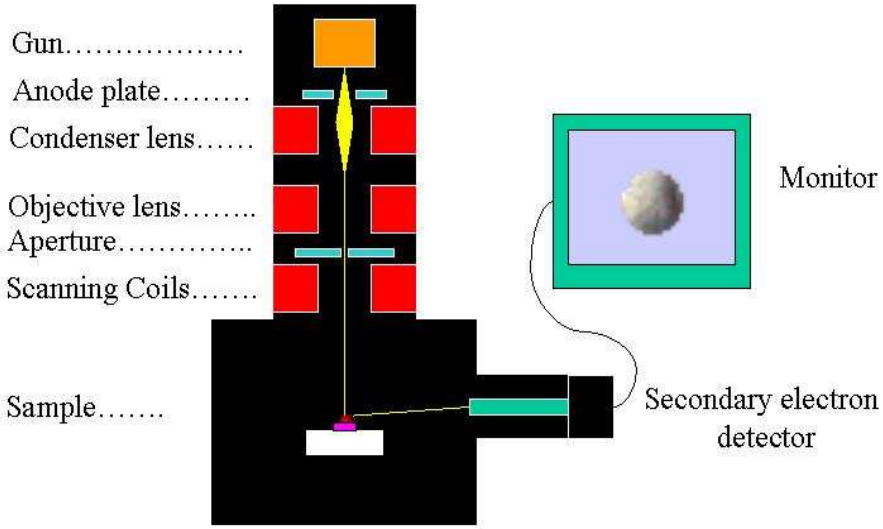

Figure 6. Layout of a basic SEM.
https://en.wikipedia.org/wiki/Scanning_electron_microscope#/media/File:Schema_MEB_(en).svg

Two scanning electron microscopies were used for imaging the fabricated ZnO and SnO_2 thin films. The TESCAN VEGA 3LMU shown in Figure 7 is located at the Department of Geosciences at UMKC. When using a tungsten heated cathode with accelerating voltage from 500V to 30kV, the achievable magnification is from 2x to 1,000,000x. The Hitachi S-570 Scanning Electron Microscope, with an LaB_6 electron gun, is located at Missouri University of Science and Technology (MST), in Rolla, MO. The accelerating voltage is from 0.5 kV to 3 kV in 100 V steps or 3 kV to 30 kV in 1 kV steps that can produce a magnification from 20x to 100,000x.

Figure 7. TESCAN VEGA 3LMU scanning electron microscopy in Department of Geosciences at UMKC.

1.6.3 Energy dispersive X-ray spectroscopy

After the discovery of X-ray radiation in 1895, the specific spectrum of radiation for each element was identified during the following four or five decades.[51] However, it wasn't until 1949 that Raymond Castaing, who was the first researcher to develop the energy dispersive X-ray spectroscopy technique, combined it with an electron microscope.[51,52]

Energy dispersive X-ray spectroscopy is an analytical technique used to acquire data about the chemical composition of a studied material. This technique takes advantage of the interaction between X-rays with matter. When a high energy beam interacts with atoms of the sample, it may excite electrons in inner shells and eject

them from the atom making the state available for another electron in the atom. When electrons from higher-energy orbits recombine with the available holes at the lower-energy states the excess energy is released in the form of X-ray photons.[51] Because each element has a unique energy structure, each element produces a unique set of peaks in its X-ray emission spectrum. From this emission spectrum the chemical composition of a sample can be identified. The energy dispersive X-ray spectroscopy technique is usually combined with electron microscopy.[49, 51] The energy dispersive X-ray spectroscopy used is A Quantax XFlash 6 | 10 made by BRUKER, shown in Figure 8, which was available for this experiment in the UMKC Department of Geosciences.

Figure 8. The energy dispersive X-ray spectroscopy detector, Model: Quantax XFlash 6 | 10 made by BRUKER from Department of Geosciences at UMKC
http://www.azom.com/images/equipments/EquipmentImage_3193.jpg

1.6.4 Ellipsometry

Ellipsometry is an optical technique for investigating the dielectric properties of materials. The technique has been known since 1888 when it was discovered by Paul Drude.[53, 54]Ellipsometry is a method based on the measurement of the change of the polarization state of light after it is reflected off of the material's surface. The change of light polarization depends on the sample's properties (film thickness, complex refractive index and dielectric function tensor). This technique can be used to measure a thin film's thickness within the nanometer range.[53-55]

An electromagnetic wave light in an ellipsometer is linearly polarized by a polarizer. It can pass through an optional compensator (retarder, quarter wave plate) before reaching the studied sample. After reflection, the radiation passes another compensator (optional) and an analyzer and falls into the detector, as shown in Figure 9. [53, 54]

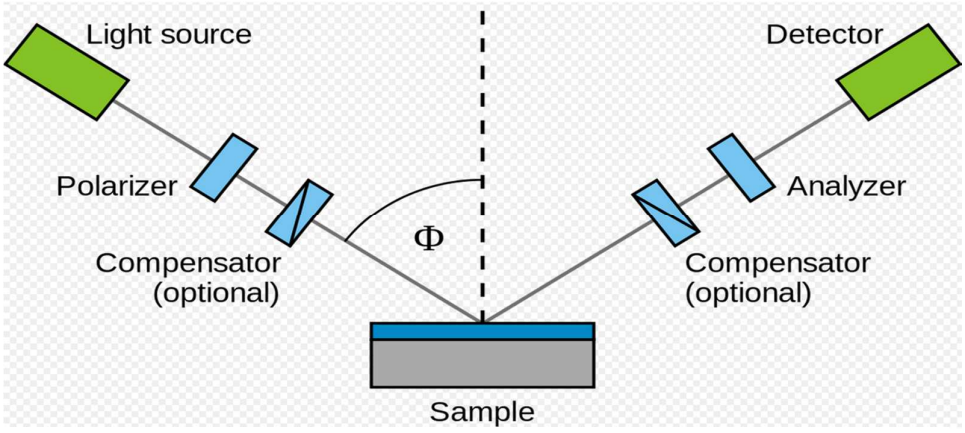

Figure 9. Layout of a basic ellipsometry system.
https://upload.wikimedia.org/wikipedia/commons/thumb/2/27/Ellipsometry_setup.svg/2000px-Ellipsometry_setup.svg.png

An ellipsometry system alpha-SE from J. A. Woollam Co is available in the UMKC Physics Department as shown in Figure 10. Ellipsometry analysis was used for gaining information about the films' thickness and indices of refraction.

Figure 10. The ellipsometry system alpha-SE from J. A. Woollam Co in UMKC Department of Physics and Astronomy.

1.6.5 Optical spectroscopy

The optical spectroscopy is a technique which uses light in the visible and adjacent ranges to analyze a material. The substances in the investigated samples will be determined by the absorption or reflectance of light in the UV-Vis range.[56] When the energy of photons passing through a semiconductor is sufficiently high, electrons in the material may be excited from the valence band to the conduction band. In result

of this transition, the photon is absorbed by the material. An edge in the absorption spectrum is observed. [56-59] Using a Tauc plot equation, the edge can be used to determine the band gap between the valence and conduction bands.[39, 42]

An ultraviolet-visible spectroscope, which is Agilent/HP 8453 UV-Visible Spectrophotometer as shown in Figure 11, at the department of physics in UMKC was used to obtain the data for calculating the bandgap energy of fabricated thin films. The light source can emit wavelengths from 190 nm to 1100 nm.

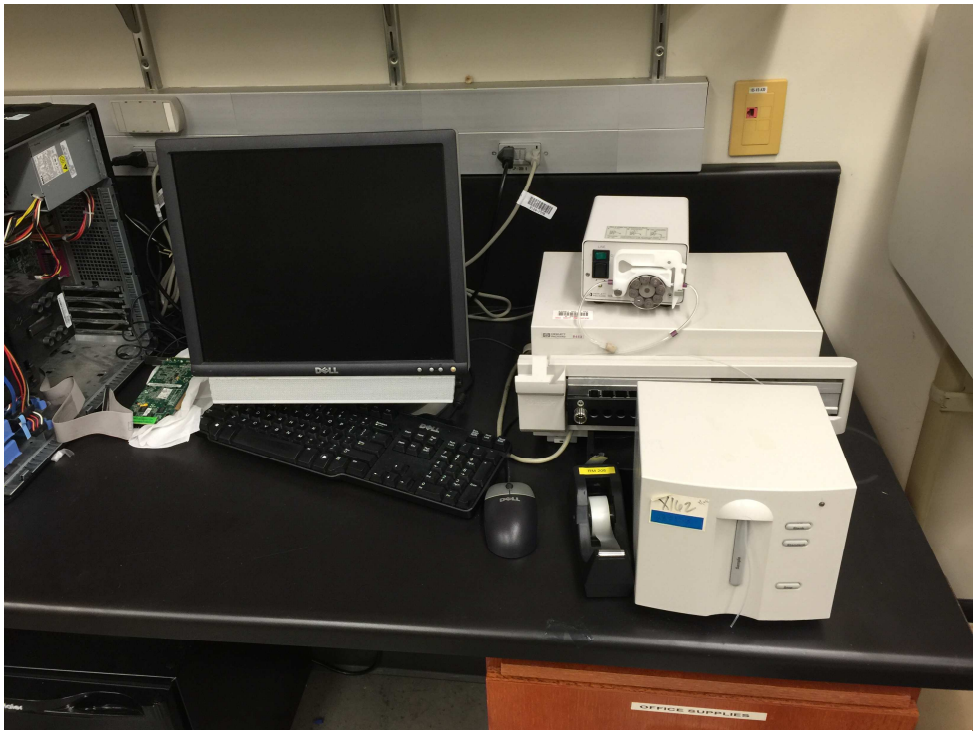

Figure 11. An ultraviolet-visible spectroscope Agilent/HP 8453 UV-Visible Spectrophotometer in the department of physics, UMKC.

1.6.6 X-ray diffraction

After the discovery of X-rays, Max von Laue, discovered that the diffraction of X-rays by crystals produces interference patterns, for which he received a Nobel Prize in 1914.[60, 61] X-ray diffraction is an analytical technique primarily used for phase identification of crystalline materials. From the diffraction pattern both the crystal structure and lattice parameters can be determined. The spacing between crystallographic planes is determined from Bragg's equation, which is discussed later.[60, 61]

The Rigaku Miniflex X-ray diffraction spectroscope system, shown in Figure 12, was available for this research at the UMKC Department of Geosciences. The system uses a copper X-ray tube with a maximum power of 600 W. Its scanning range

Figure 12. The Rigaku Miniflex X-ray diffractometer at the UMKC Department of Geosciences.

is from -3 to 145º (2θ), scanning speed from 0.01 to 100º/min (2θ) and minimum step width 0.005º. For this research, the scanning range is from 30º to 60º (2θ), count time is 3 seconds and minimum step width is 0.05 º.

1.6.7 Raman spectroscopy

The Raman effect, which is a type of inelastic scattering of light waves, was initially discovered by C.V. Raman, an Indian scientist for which the phenomenon was named after. Raman spectroscopy is a powerful technique that is mainly used to identify or characterize different and unique vibrational modes for simple and complex molecules.[57] The continued improvement of excitation sources such as lasers and trace stand-off detection, as well as the possibility of studying materials in gaseous, liquid or solid phases made Raman spectroscopy a popular technique in academic, industrial, or military research. The Raman effect occurs by irradiating a sample with an intense-monochromatic light (typically lasers in the UV-vis range). The photons from the light source interact with the sample by either transferring (Stokes) or receiving (anti-Stokes) some energy to the molecules in the sample.[57, 59] The energy transfer results in phonons or vibrations being produced in the sample and the incident photons to be (inelastically) scattered with a different energy (either lower or higher). The energy difference, usually called the Raman shift, is determined with respect to the excitation source. Currently, the 514.5 argon-ion green laser line is the most commonly used light in Raman spectroscopy.[62] These Raman shifts correspond

to different vibrational modes in the material and are dependent upon the types of bonds and atoms that comprise the molecules within a sample. On average, only one photon per 10^6 incident photons is inelastically scattered via the Raman effect. Hence, intense excitation light sources are needed. [57, 59, 62]

CHAPTER 2

BACKGROUND

2.1 Lambert-Beer-Bouguer law

An energy transfer process governing Pulsed Laser Deposition must follow the energy conservation law. When the laser beam interacts with transparent materials, the energy carried by the laser light will separate into reflected energy, absorbed energy and transmitted energy. Therefore the following equation must be satisfied:

$$1 = \frac{E_r}{E_0} + \frac{E_a}{E_0} + \frac{E_t}{E_0} = R + \alpha + T \tag{2.1}$$

where E_0 is the energy carried by the incident light, R is the reflection rate; α is the absorption rate; and T is the transmission rate of the material. For an opaque material, there is only reflected energy and absorbed energy. For an opaque material, the equation (3.1) changes to:

$$1 = R + \alpha \tag{2.2}$$

If I is the laser intensity and dI is the reduction of the intensity as the light passes through a thickness of target, dx, then

$$\frac{\mathrm{dI}}{\mathrm{I}} = -\alpha \mathrm{dx} \tag{2.3}$$

$$\alpha = \sigma \mathrm{N} \tag{2.4}$$

Where the proportionality constant α, is known as the absorption coefficient, σ, is the absorption cross section, and N is the density of the material.

Integrating equation 3.3 from the surface to a depth x below the surface yields[44]:

$$\mathrm{I} = I_0 e^{-\alpha x} \tag{2.5}$$

Equation (3.5), known as the Lambert-Beer-Bouguer Law, indicates that as light passes through a material its intensity deceases exponentially with the distance travelled in the material.

Absorption of a photon occurs only when the energy of the photon precisely matches the energy difference between the initial and final states. In the interaction of incident radiation with matter, if there is no pair of energy states that matches the photon energy, the photon cannot be absorbed and the matter will be "transparent" to that radiation. The absorption of light, between two states E_1 and E_2, follows the equation[63]:

$$\Delta E = E_2 - E_1 = h\upsilon = \frac{hc}{\lambda} \tag{2.6}$$

absorption is "allowed" when the energy of the photon, *hv*, is equal to the energy difference between the two states.[63, 64]

2.2 Thermal effects in laser ablation

The thermal effects in laser ablation include surface evaporation, melting and phase explosion.[26] The following equation is a simplified model describing the temperature distribution during the evaporation and melting of a surface [26, 65]:

$$c(T)\rho(T)\frac{\partial T}{\partial t} = \frac{\partial}{\partial x}\left(K(x,T)\frac{\partial T}{\partial x}\right) + \alpha I(x,t) \tag{2.7}$$

Where T is the temperature, x is the depth at time t; αI is the absorbed laser intensity as indicated by the Lambert-Beer-Bouguer Law; c , ρ and K the thermal capacity,

density and thermal conductivity of the target material. For simplicity ρ and K are frequently assumed to be temperature and space independent.[26]

When surface melting takes place, the solid-liquid phase transition must be included in the analysis. To consider the transition during laser irradiation, two boundary conditions are required at the interface where the phase transition occurs. Combining the boundary conditions with conservation of energy ($J = -K\nabla T$) results in [26]:

$$\rho \Delta H_m(T_{tr}) v_{int} = K_{solid} \frac{\partial T}{\partial x}\Big|_{x^+ int} - K_{liquid} \frac{\partial T}{\partial x}\Big|_{x^- int} \tag{2.8}$$

Where T_{tr} is the temperature of the superheated target; K_{solid} is its thermal conductivity; K_{liquid} is the thermal conductivity of the liquid phase; ΔH_m is the heat of fusion at T_{tr}; v_{int} is the velocity at the solid-liquid interface, which is a function of $T_{tr} - T_m$, with T_m being the melting temperature of the target material, which can be written generally as [26]:

$$v_{int} = f(T_{tr} - T_m) \tag{2.9}$$

Due to surface evaporation, the target's surface recedes at a velocity v_r as shown in Figure 13. Suppose a reference frame is positioned such that the target's surface is at x=0. The temperature dependence from equation (2.7) becomes[26]:

$$c\rho \frac{\partial T}{\partial t} = K \frac{\partial^2 T}{\partial x} + c\rho v_r \frac{\partial T}{\partial x} + \alpha I(x,t) \tag{2.10}$$

An estimation of the recession velocity of the target surface v_r needs to be taken into consideration for both the temperature and the pressure in the liquid phase. In result

the number N_v of the particles evaporating per unit time and area can be expressed by the following[26, 65]:

$$N_V = \frac{p}{(2\pi kTm)^{1/2}} C_s \tag{2.11}$$

Where p is the gas pressure, m is the molecular mass of the target material and C_s is their sticking coefficient.[26]

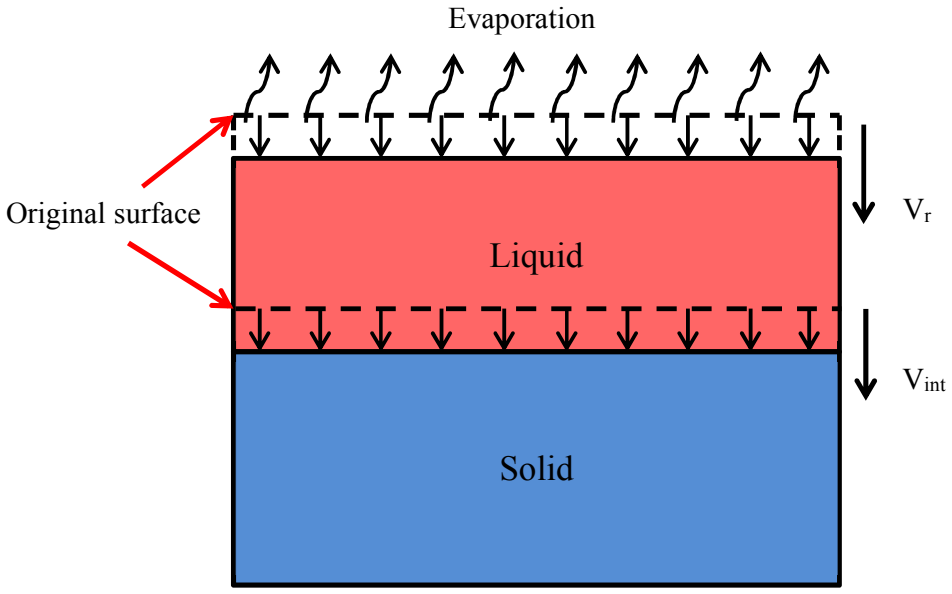

Figure 13. Evaporation process and surface recession velocity V_r, the solid-liquid interface velocity V_{int}

For high intensity pulses, phase explosion will occur when temperature rises at a rate of ~10^9 K/s. At this point, the melted layer on the target surface changes its state from stable to metastable. In the vicinity of critical temperature of ~0.9 T_c, homogeneous nucleation causes: intensive bubble formation, energy release, and formation of a foam consisting from liquid droplets and vapor.[29] This explosive process is also called phase explosion, where the rate of homogeneous nucleation

increases in a short period of time.[29, 65] In other words, the temperature of the liquid becomes higher than the boiling temperature. This increase of homogeneous nucleation rate causes shifts from the bimodal states into the metastable states. If a target is ablated, the relationship between vapor pressure and temperature of the target material is described by the Clausius-Clapeyron equation:

$$\ln(\frac{p_1}{p_2}) = \frac{\Delta H_{vap}}{R}(\frac{1}{T_2} - \frac{1}{T_1}) \tag{2.12}$$

where p_1 and p_2 are the pressures at two temperatures T_1 and T_2, and R is the universal gas constant.[26, 66]

2.3 Thin film growth

Both nucleation and growth of crystalline films depend on many factors such as the density, absorption energy, degree of ionization, and the type of the condensing material. Nucleation and growth of crystalline films also depend on the temperature and the physical-chemical properties of the substrate. The two main thermodynamic parameters for the growth mechanism are the substrate temperature T and the supersaturation Δm. They can be related by the following equation:

$$\Delta m = kTln\left(\frac{R}{Re}\right) \tag{2.13}$$

where k is the Boltzmann constant, R is the actual deposition rate, and Re is the equilibrium deposition rate at temperature T.[8, 30]

2.4 Band gap energy

In this research, two semiconductor targets have been used to make thin films. For semiconductors, the band occupied by valence electron is called the valence band and the band occupied by free electrons is called the conduction band.[67] In order for a bound electron to become a free electron, it must obtain sufficient energy to make this transition from the valence band to the conduction band. The minimum energy needed for this transition is called the band gap energy. Band gap means the energy difference between the lowest energy level at the bottom of conduction band and the highest energy level at the top of valence band. The band gap of a semiconductor can be either a direct band gap or an indirect band gap. Each energy state in the conduction band and each energy state in the valence band corresponds to a certain crystal momentum (k-vector) in the Brillouin zone.[39, 67] If the k-vectors of the bottom of the conduction band and the top of the valence band are equal, meaning the momentum of electrons and holes is the same in both the conduction band and the valence band, as shown in Figure 14(a), the band gap is direct. If the k-vectors of the electrons at the bottom of the conduction band and the holes in the valence band are different, as shown in Figure 14(b), the band gap is indirect. In a transition across a direct band, electrons can absorb or emit photons without additional effects taking place in the semiconductor. In an indirect band gap semiconductor, the electron must transfer some of its momentum to the crystal lattice during the transition.[67-69]

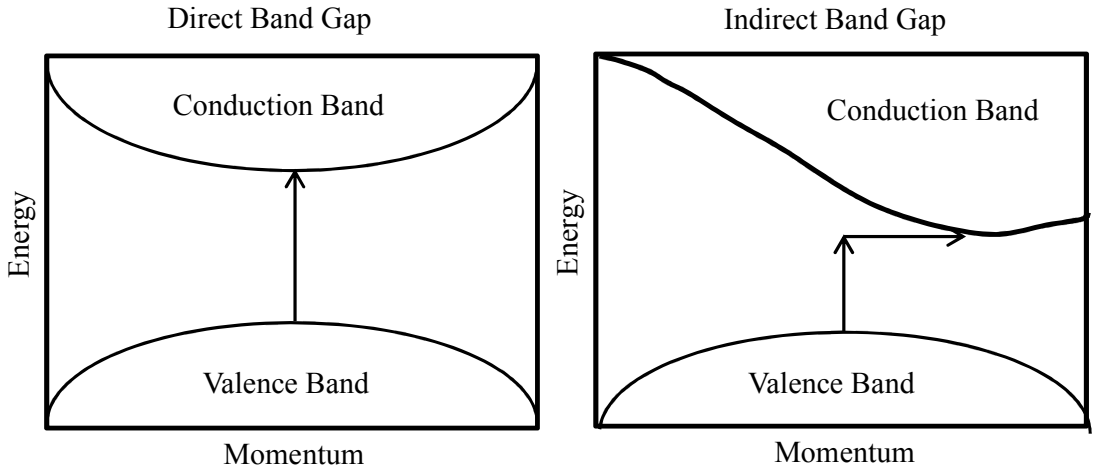

(a). Direct band gap (b) Indirect band gap

Figure 14. Two types of band gap.

Band gap is an important parameter for characterizing the properties of semiconductor materials. First of all, the band gap energy is a reflection of the strength of the bond for valence band electrons. Secondly, the band gap represents the potential difference between the electrons and holes. The bottom of conduction band can be treated as a potential energy of free electrons. The top of the valence band can be treated as a potential energy of the bound electrons. Lastly, the band gap reflects the electrical and optical properties of the materials.[67, 69, 70]

In this research, optical spectroscopy is used to determine the band gap energy of the semiconductor thin films. When light with a certain wavelength enters a semiconductor thin film, valence electrons may undergo a transition from a lower energy state to a higher energy state by absorbing the photon energy. The energy, E_{photon}, of a photon must be equal to or greater than the band gap E_g of the semiconductor

$$E_g = hv_0 \tag{2.14}$$

where v_0 is the threshold frequency of material.

Since the reflectivity of the studied materials in the ultraviolet and visible light region is relatively small, the effects of the reflectance can be ignored and the absorption coefficient α could be related to the thickness of the film d and the measured transmittance T by:

$$\alpha d = \ln(1/T) \tag{2.15}$$

The optical band gap of a semiconductor can be evaluated from the absorption spectrum using the Tauc relation[71]:

$$(\alpha hv) = C(hv - E_g)^{\frac{m}{2}} \tag{2.16}$$

$$C \approx \frac{e^2(2\mu^*)^{3/2}}{nch^2me^*} \tag{2.17}$$

where C is a constant which depends on the type of the band gap, h is Planck's constant, α is the absorption coefficient, E_g is the average band gap of the material, m is a number dependent on the type of transition, n is the refractive index, $\mu^*$is the reduced mass of the electrons and holes, and c is the speed of light.[71] Since this research is focused on the direct band gap of semiconductor thin films, for which m=1, equation (2.19) can be simplified to:

$$(\alpha hv)^2 = C^2\left(hv - E_g\right) \tag{2.18}$$

For the determination of the band gap equation (3.21), we need to create a Tauc plot of $(\alpha hv)^2$ versus frequency, and linearly extrapolate the function to the zero value.

The extrapolation crossed the abscissa at the threshold frequency of the thin film material.[68, 71]

It is necessary to indicate that the entire pulsed laser deposition system design and set up is a part of this dissertation work. The following chapter will introduce details about this pulsed laser deposition system.

Chapter 3

Experimental Procedures

3.1 Set up

3.1.1 Pulsed laser deposition system design

A Pulsed Laser Deposition (PLD) system can be separated into several subsystems. First, an appropriate laser for the desired application must be selected. Due to the nature of the material used in this project, an excimer pulsed laser was chosen for the PLD of the studied materials. Depending on the working gas being used in the laser, the wavelength of its radiation can vary from 193 nm to 351 nm in the ultraviolet region.[8] Within this range, the absorption coefficient of the studied target materials is sufficiently high making ablation of the target material possible. The second aspect of the system is the vacuum system, which includes a processing chamber, vacuum pumps and pressure sensors. This subsystem can provide an appropriate vacuum environment for the deposition. A target stage with a rotational mechanism make up the third subsystem. Finally, the substrate holder and an appropriate substrate heater constitute the fourth subsystem. A schematic diagram of the entire PLD system is shown in Figure 15.

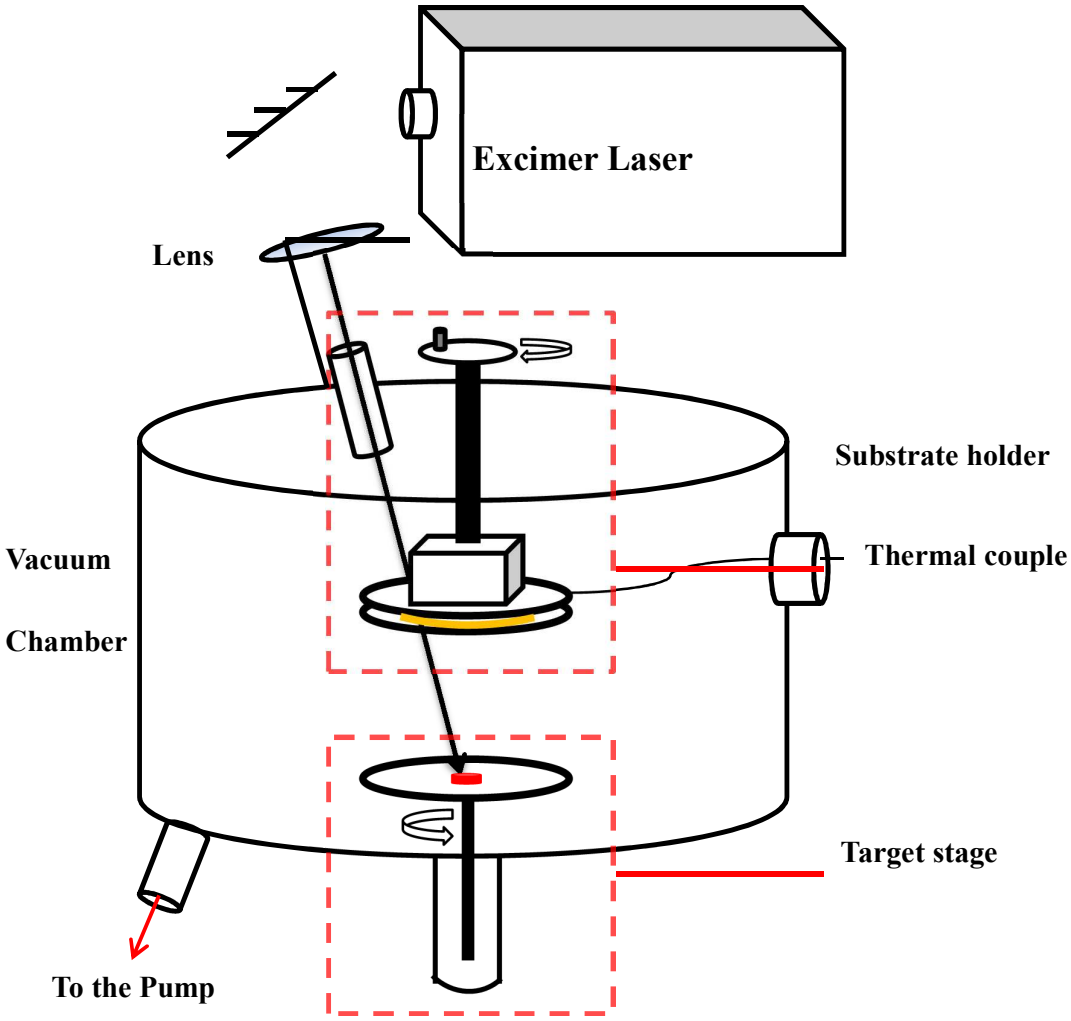

Figure 15. Schematic diagram of the PLD system

3.1.2 Laser

For this research, a Coherent COMPexPro excimer laser, shown in Figure 16, was used. The active medium in this excimer laser is a mixture of a halogen gas (F_2 / Cl_2) and a noble gas (Ar / Kr / Xe). Depending on the selected working gas, the laser can emit radiations with wavelength of 193nm (ArF), 248 nm (KrF), 308 nm (XeCl)

and 351 nm (XeF). In all options, the laser produces 20 ns or 25 ns pulses with energy varying from 100 mJ to 700 mJ. The maximum repetition rate can vary from 10 Hz to 100 Hz. For the purpose of the project, the laser operated at 351 nm, maximum frequency of 10 Hz and maximum pulse energy of 300 mJ.

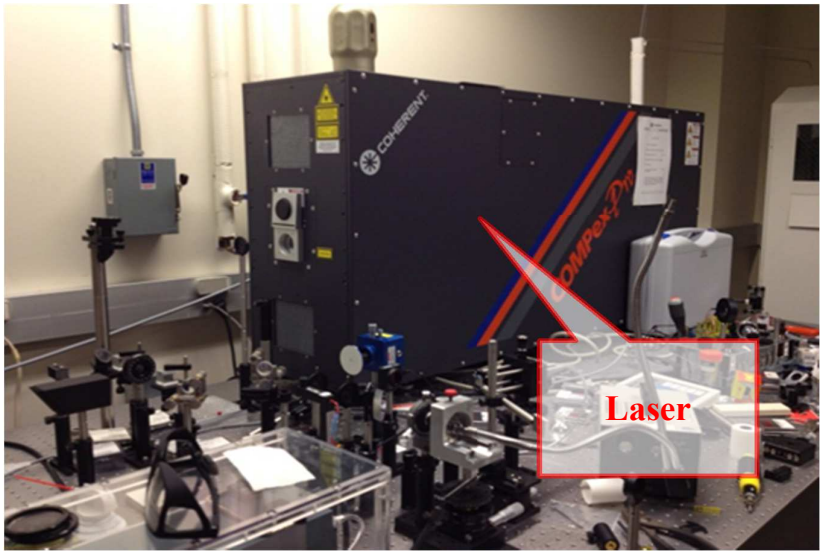

Figure 16. Photograph of the laser used in this work.

As shown in Figure 17, the constructed set-up uses dielectric mirrors and a lens to direct the beam on the target. Focusing this beam to a 100 µm diameter spot

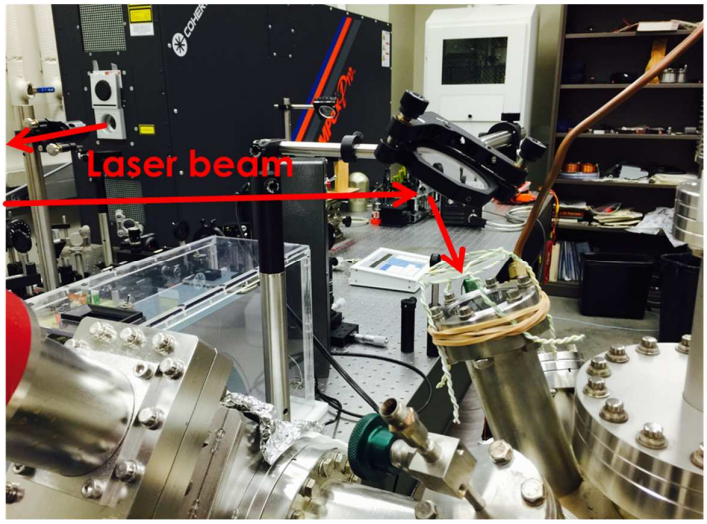

Figure 17. Dielectric mirrors and a lens will direct the beam into chamber.

resulted in a fluence of approximately 400 J/cm^2, which exceeds the necessary fluence for the laser ablation of the target materials in this project.[72]

3.1.3 Vacuum system

The vacuum subsystem includes a multi-port vacuum chamber, two vacuum pumps and pressure sensors. The high-vacuum processing chamber, used in this project, was assembled from ConFlat high vacuum components. The main chamber has six ports for the target and substrate stages, power supply, laser beam delivery, connecting sensors, and evacuating of the chamber.

High vacuum was achieved using a turbo-molecular pump, with which pressure below 10^{-9} Torr can be attained with room temperature. Operation of the turbo-molecular pump (Figure 18) also requires a mechanical pump, with which pressure in the chamber can be reduced to 10^{-3} Torr.

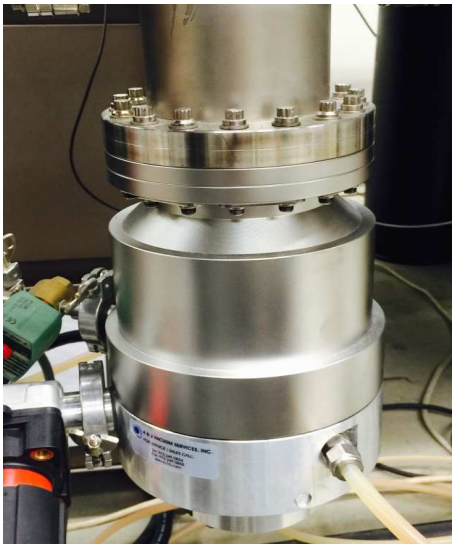

Figure 18. Turbo Pumps

Hot-filament ion gauge, connected to a control unit with a digital display, was used as the pressure sensor.

After the vacuum chamber is set up, it is necessary to clean the entire vacuum chamber. If the vacuum chamber is not clean, the vacuum cannot be reached well because of air molecules or oil from finger prints on the inner surface of the chamber. There are several steps that are used to clean the vacuum chamber. The first step is using ethanol then acetone to wash the vacuum chamber. Then finally, the chamber must be baked for a long time with all the pumps running. After the chamber is cleaned, the vacuum level will have a change in pressure from 10^{-6} Torr to 10^{-9} Torr. This pressure satisfies the conditions for pulsed laser deposition of thin films.

3.1.4 Target stage

At the beginning of designing the target stage, there was a problem that needed to be solved. The problem was producing a constant laser ablation rate without breaking the vacuum environment inside the chamber. A constant ablation rate was achieved by making the target stage rotate. In order to rotate the target stage in a vacuum environment, there needs to be a non-contact force which provides this motion. A small piece of a magnet inspired me with an idea, which was using magnetic force in order to rotate the sample.

To have uninterrupted laser ablation the source target had to be mounted on a rotational stage. Since the pulsed laser deposition process happened in a vacuum

environment, a magnetic coupler (shown in Figure 19) delivered appropriate torque to the target stage. The target stage system consists of two separate rotors with magnets. A small stepper motor drives the outer rotor around the target stage port by providing a magnetic torque to the inner rotor to which the stage is mechanically connected. The coupler made it possible to rotate the target without breaking the vacuum environment inside of the chamber. The rotation of the target stage ensured the target material was ablated at a constant rate.

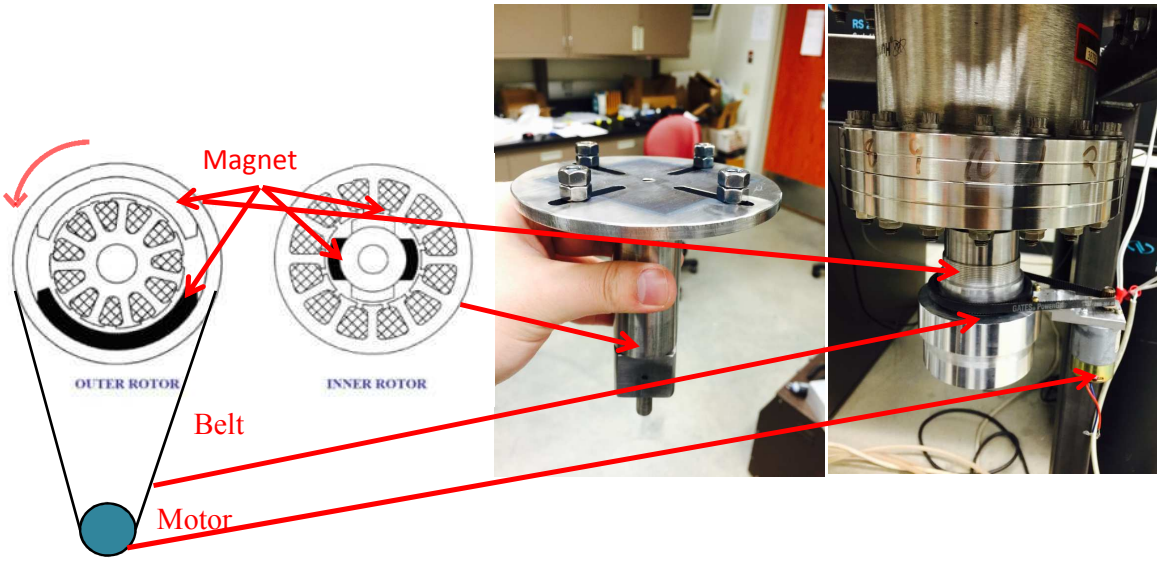

Figure 19. Target stage. A stepper motor drives the outer rotor, which is magnetically coupled to the inner rotor attached to the target stage.

3.1.5 Substrate holder and substrate heater

The substrate system includes a substrate holder and a substrate heater. The design of the system is shown in Figure 20. The film substrate is held by a fastener made from two plates attached with four screws to a plate that is connected to the shaft. In order to monitor substrate temperature, a thermocouple is inserted into the fastener. Two halogen lamps, seen in Figure 21, behind the plates serve as the heat source for adjusting the temperature of the substrate during the deposition process. The heater can maintain the temperature of the substrate up to 1000 ºC. This entire system is fixed on a linear shaft shown in Figure 22 making the distance between the target stage and substrate holder adjustable.

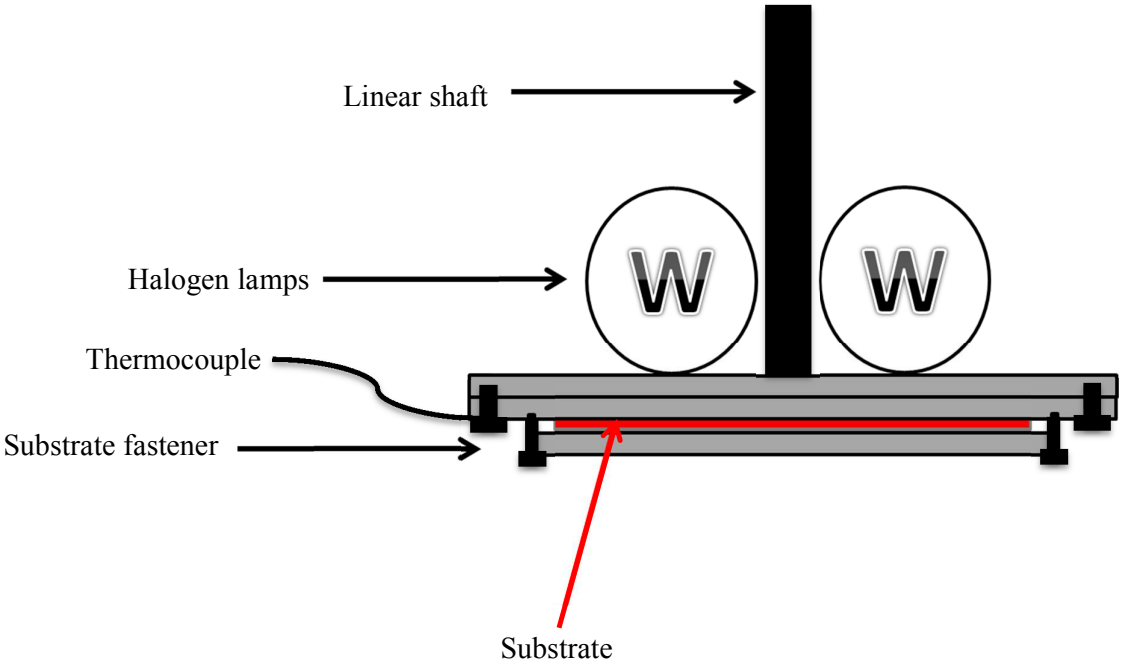

Figure 20. Substrate holder and substrate heater

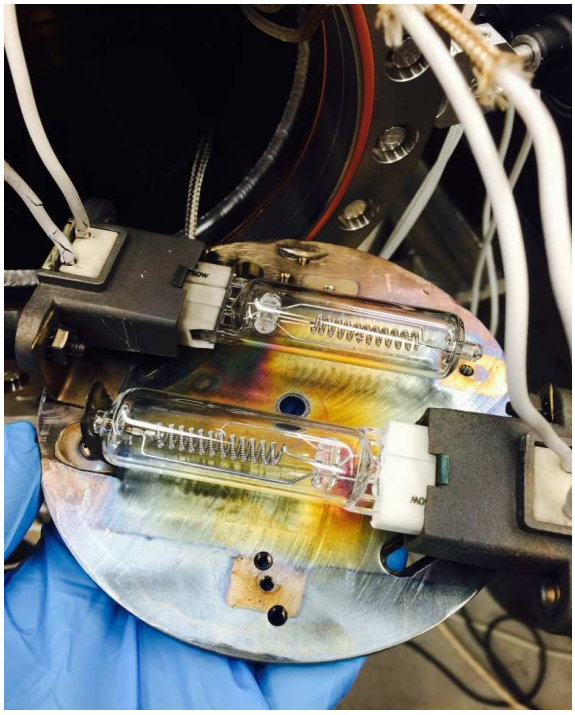

Figure 21. Halogen lamps provide heat to the back of the target holder.

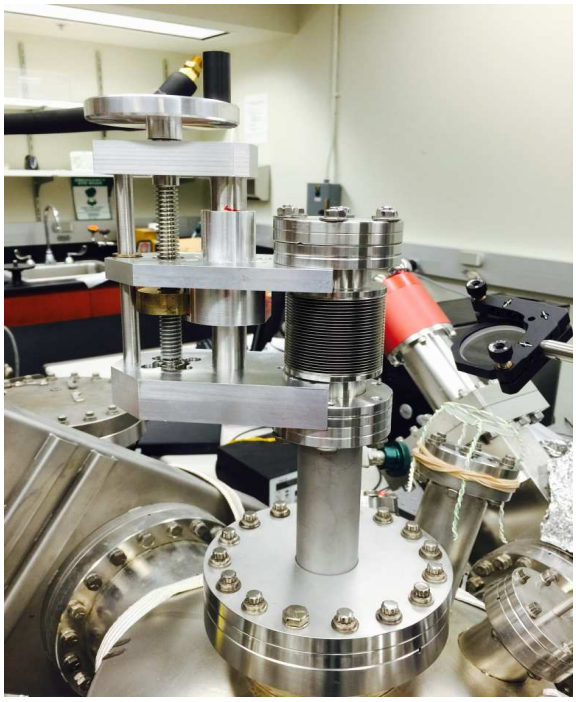

Figure 22. Linear shaft vertical positioning of the target is accomplished by using the adjustment screw to the left.

CHAPTER 4

DATA COLLECTION AND ANALYSIS

4.1 Sample preparation

The depositions of both ZnO and SnO_2 thin films were carried out under different substrate temperatures, laser fluencies and pressures in the chamber. The zinc oxide thin films were prepared under pressures on the order of 10^{-5} Torr and the laser pulse energy was kept around 200 mJ. The distance between the substrate holder and target stage was 3.5cm, and the laser pulse frequency was set at 5Hz. The SnO_2 thin films were prepared under pressures on the order of 10^{-5} to 10^{-6} Torr, and the laser pulse energy was kept around 200 mJ. The distance between the substrate holder and target stage was 3.5cm or 5cm, and the laser pulse frequency was set at 5Hz. Before the laser beam reached the target material it passed a convex lens with a wavelength range of 350-2000nm and a focal length of 300 mm. With help of this lens, the laser beam can be focused to a spot as small as 60 microns in diameter. This makes sure that the fluence of the laser beam can reach up to 148.62 J/cm^2, which is higher than the laser ablation thresholds of ZnO (0.44 J/cm^2) and SnO_2 (0.73 J/cm^2).[73]

The thicknesses of the thin films were measured using ellipsometry. For selected samples, the thicknesses measured with ellipsometry were verified using scanning electron microscopy. The SEM images, EDS spectrum, XRD spectrum, UV-Vis spectrum and Raman spectrum were also used for analysis. SEM images were also

used to observe the surface morphology. The EDS spectrum was combined with the SEM images which were used for the elemental analysis and chemical characterization of the thin film sample. The XRD diffraction and Raman spectroscopy were used to check the crystal structure of the thin films. The UV-Vis spectroscopy was used to obtain optical absorption information of the fabricated thin films, then this information was used to calculate the band gap energy of the thin films.

4.2 ZnO thin films

The conditions of the ZnO film preparation as well as the deposition time and thickness of the films are listed in following tables, each table has its specific substrate temperature with other various parameters.

Numbers of the ZnO thin films were fabricated at 300 ºC and shows in table 1:

Table 1. Growth condition and thickness of ZnO thin films at 300 ºC part 1

	Pressure (Torr)	Laser energy (mJ)	Distance (cm)	Time (min)	Thickness (nm)	Ablation rate (nm/min)
1	1.4×10^{-6}	220	3.5	30	13.92	0.46
2	1.7×10^{-6}	202	3.5	30	--	--
3	1.3×10^{-5}	181	3.5	30	25.46	0.85
4	1.4×10^{-5}	163	3.5	30	21.86	0.73
5	1.3×10^{-5}	199	3.5	30	--	--
6	1.5×10^{-5}	210	3.5	30	41.00	1.37
7	1.5×10^{-6}	190	3.5	45	25.96	0.58
8	1.6×10^{-6}	226	3.5	45	39.88	0.89
9	9.9×10^{-6}	194	3.5	45	56.03	1.25
10	1.3×10^{-5}	171	3.5	45	60.26	1.34
11	1.5×10^{-6}	206	3.5	60	53.24	0.89
12	1.4×10^{-6}	231	3.5	60	82.25	1.37
13	1.5×10^{-6}	228	3.5	75	91.94	1.23
14	1.5×10^{-6}	199	3.5	75	65.99	0.88
15	1.6×10^{-6}	199	3.5	90	77.41	0.86
16	1.7×10^{-6}	234	3.5	90	112.11	1.25

-- Data not acquired.

Table 1. Growth condition and thickness of ZnO thin films at 300 ºC part 2

	Pressure (Torr)	Laser energy (mJ)	Distance (cm)	Time (min)	Thickness (nm)	Ablation rate (nm/min)
17	6.6×10^{-6}	166	5	45	--	--
18	6.8×10^{-6}	179	5	75	24.35	0.32
19	6.9×10^{-6}	164	5	90	15.07	0.17

-- Data not acquired.

The data that was acquired shows that when there is a longer the distance between the substrate heater and the target stage the ablation rate is lower. When the distance is 5cm the ablation rate is less than 0.32nm/min. However, if the distance is 3.5cm the ablation rate is higher than 0.5nm/min. This occurs because the laser induces a plasma plume and the size of plasma plume is decided by the free path of the particles inside of the plasma. The pressure is mainly what effects the free path within the plasma plume. Since the pressure was around the order of 10^{-5} to 10^{-6} Torr, the size of the plasma plume was similar for each sample. Therefore, the lower ablation rate can be attributed to the longer distance between the substrate heater and the target stage because this allows fewer particles to reach the substrate during the free expansion of the plasma plume.

Generally speaking, as time increases, the thickness of the thin film will increase too. However, the laser pulse energy also has an effect on the thin film's thickness

while all the other parameter are the same. For example, the data retrieved for 30mins of deposition for sample 3, sample 4 and sample 6 leads to conclusion that high laser energy produces a higher laser ablation rate. Consistently, the same trend was observed in several sample pairs: sample 7 and sample 8, sample 11 and sample 12, sample 13 and sample 14, sample 15 and sample 16. For better explanation, the pair, sample 13 and sample 14, was selected for more details. This pair of ZnO thin films were fabricated under the same pressure of 1.5×10^{-5} Torr, at the same substrate temperature of 300 ºC and the same deposition time of 75 minutes. The only difference between the two samples was the laser pulse energy. Sample 13 was grown at energy of 228 mJ, and sample 14 was grown at a lower energy of 199mJ. In result, sample 13 is thicker than sample 14. Since the pressure for each sample was similar, the laser ablation rate was only affected by the laser pulse energy. This means the number of ejected particles was correlated with the laser pulse energy.

The ZnO thin film (sample 13) cross-section is shown in Figure 23 (a). The image confirms the information on the thickness if the film that was obtained in the ellipsometric measurements. It is seen that throughout its volume, the film is uniform with no visible grain boundaries. The film surface of the sample is shown in Figure 23 (b). The surface is smooth with no observable morphological features. The similar surface structure acquired from majority of the ZnO thin film samples in table 1.

(a)

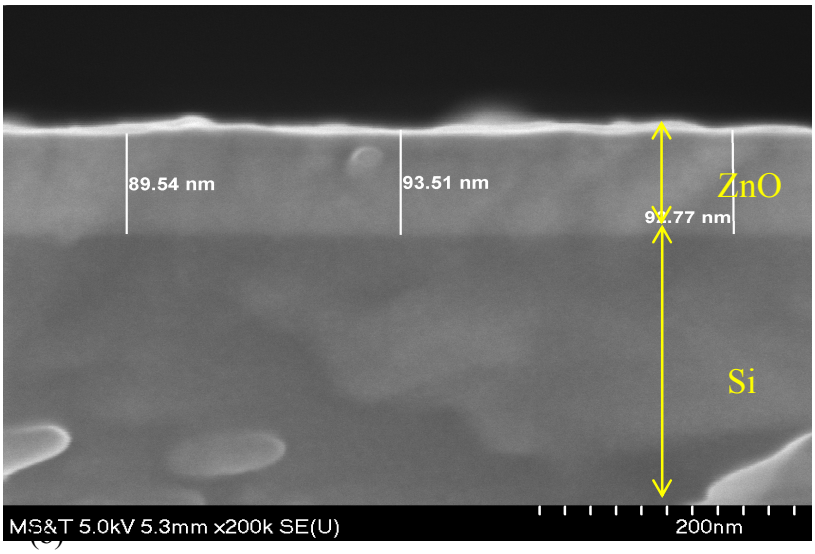

(b)

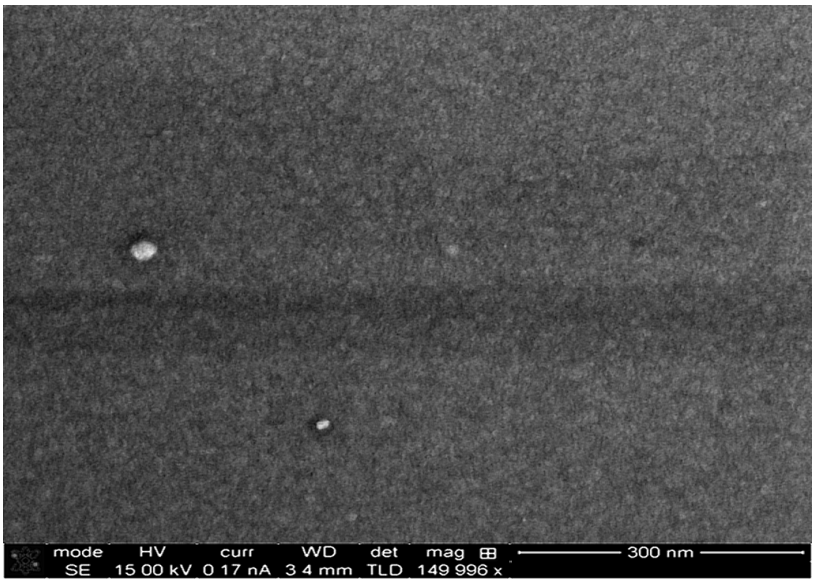

(a) The cross-section of a ZnO thin film (sample 13)
(b) The surface of a ZnO thin film (sample 13)

Figure 23. ZnO thin film deposited on a Si wafer with 228 mJ, 75 mins.

Figure 24 shows the distribution of both Zn and oxide across the surface of sample 11 obtained through the EDS. Figure 25a shows the SEM image of the investigated area. In Figure 15b, the red dots represent Zn and green O, respectively.

Each of the elements has a uniform distribution which supports the hypothesis that the ZnO film is formed on the surface.

(a)

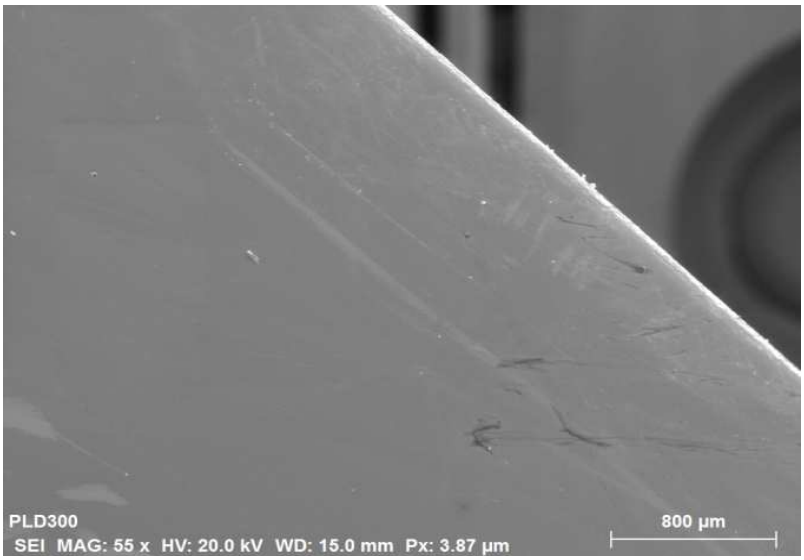

(b)

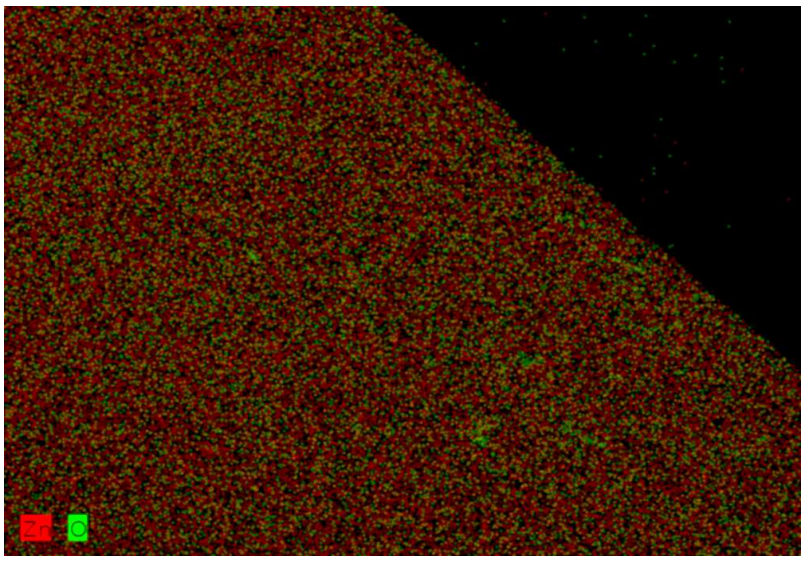

(a) SEM image
(b) EDS map image
Figure 24 Sample 11, 1.5×10^{-5} Torr, 300 ºC, 206 mJ and 60 mins.

In Figure 25, the EDS spectrum together with the quantitative analysis of the EDS data collected from sample 11 is presented. In the spectrum, the Si signal from the substrate and C signal from the adsorbed Carmon compounds are observed in addition to Zn and O signals. The difference in the atomic fraction of Zn and O can be explained by presence of other oxides on the studied surface. The silicon wafer was oxygenized by the environmental air which contains both O_2 and CO_2. The fact that the air contains CO_2 also explains the presence of carbon on the sample.

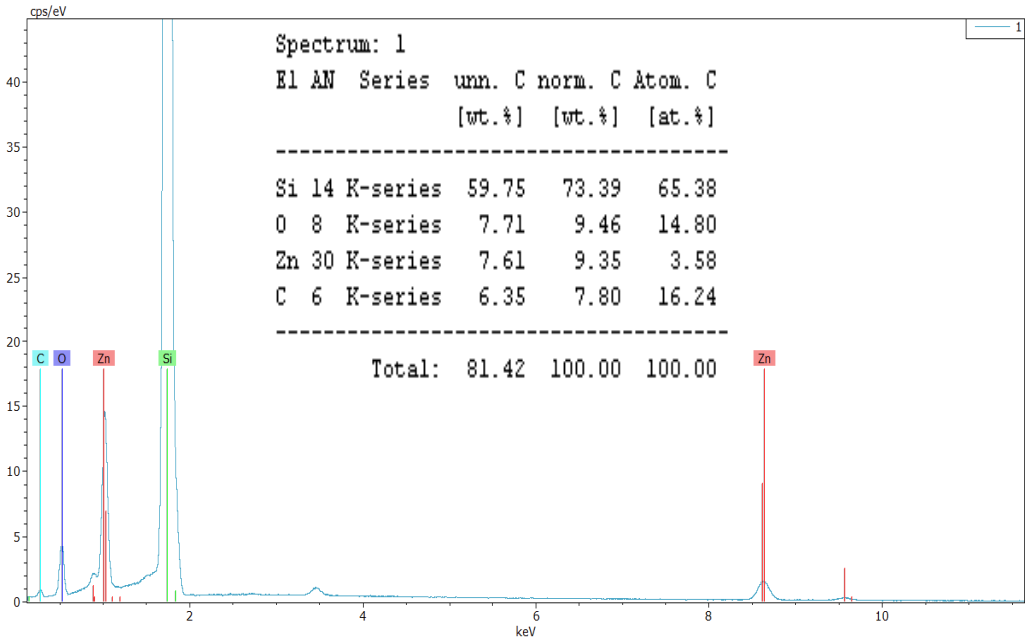

Figure 25 EDS spectrum of sample 11, 1.5×10^{-5} Torr, 300 ºC, 206 mJ and 60 mins.

Raman spectra, collected with A Spex 1403 double monochromator and a 514.5 nm laser excitation at a 90º scattering angle, were also used to evaluate the crystalline structure of the films. Figure 26 represents an example of the Raman spectrum obtained for sample 13. Based on the ZnO reference, the spectrum of thin

films typically have six peaks corresponding to the longitudinal optical (LO) phonons. The 586 cm^{-1} peak, observed in this experiment, corresponds to the first longitudinal optical (LO) mode of crystalline ZnO identified in previous studies of the others.[74, 75] The peak occurring at 519.5 cm^{-1} is from the Si substrate on which the thin film was deposited on. A higher LO mode of ZnO were detected but were not substantial for the purposes of characterization in this study and therefore are not reported here.

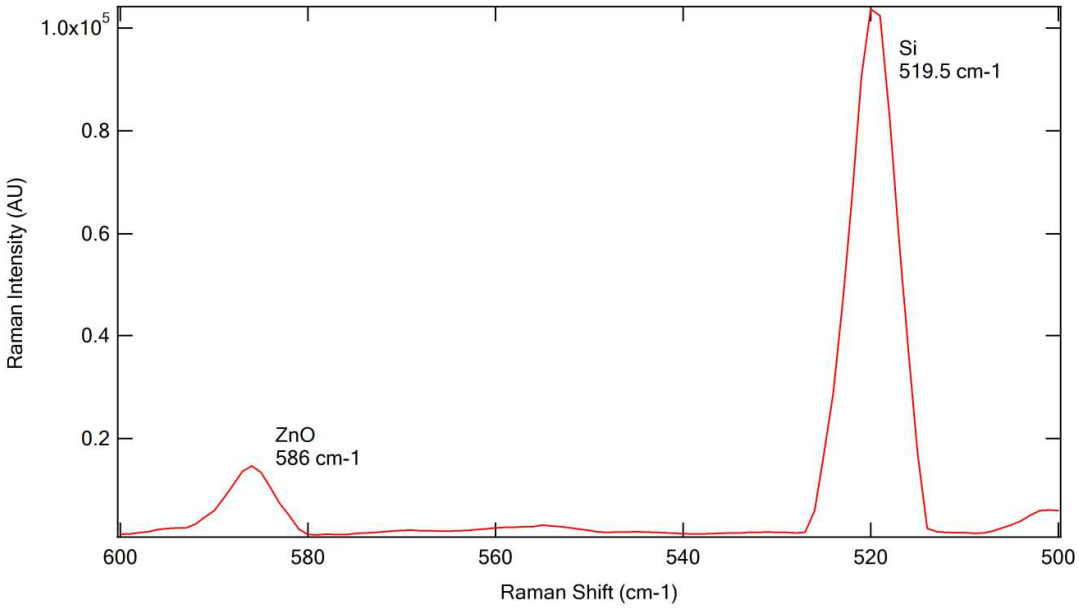

Figure 26 Raman spectrum of sample 13,
1.5×10^{-5} Torr, 300 ºC, 228 mJ and 75 mins.

XRD was used to obtain information about the crystalline structure of the films. The spectrum which was acquired by the XRD for sample 12 is shown in Figure 27, and a typical XRD pattern for ZnO thin films is shown in Figure 28. There is only a single peak in Figure 28, which is created by a particular family of planes in the crystalline structure of the sample. Comparing the spectrum obtained in this experiment with the typical XRD spectrum indicates that the peak can be associated with the (002) family of crystallographic planes. The XRD experiment performed on other samples grown at 300ºC yielded a similar single peak corresponding to the (002) orientation. However, if the film was too thin like that of sample 1 or sample 19, it did not indicate crystallinity. This may mean that from the initial growth of ZnO on silicon, the effect of interface results in an amorphous film. Only after a sufficient buffer layer is formed, does the film have the appropriate conditions to crystalize.

Most research indicates that a higher substrate temperature is required to create a high quality crystalline ZnO thin film.[7] In the past decade, there are some reports from other researchers interested in using lower temperatures between 300 ºC and 500 ºC for pulsed laser deposition of ZnO thin films.[22,76] There are reports of growing high orientation ZnO thin films and ZnO nanoparticles on the substrate at 350 ºC.[8, 23, 37, 76] Thus, these previous reports made me curious about how a lower temperature pulsed laser deposition affects the crystalline structure of ZnO thin films. Several lower temperature settings have been attempted for fabricating ZnO thin films by this pulsed laser deposition system.

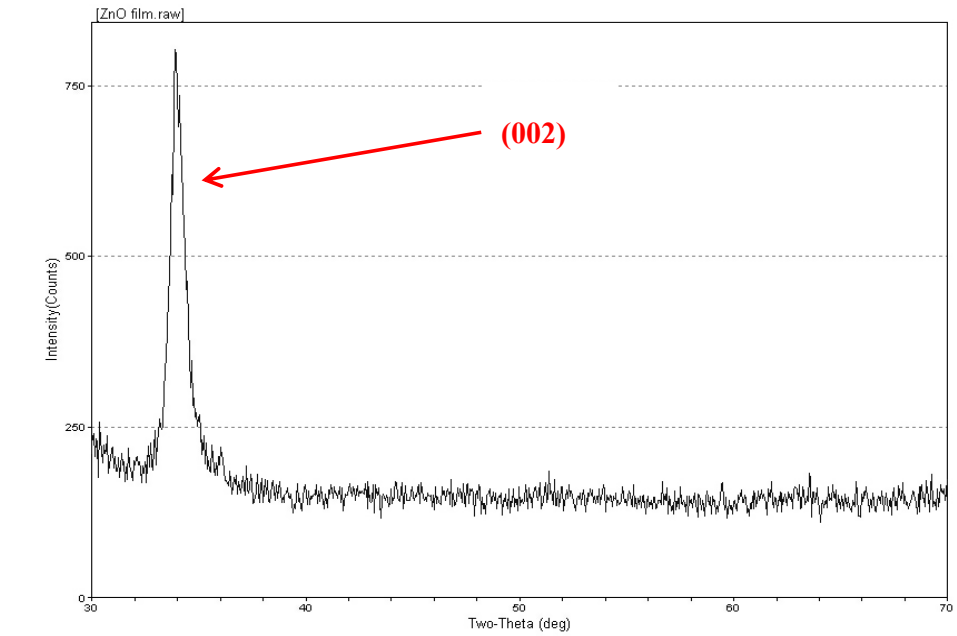

Figure 27 XRD spectrum of sample 12,
1.5×10^{-5} Torr, 300 ºC, 231 mJ and 60 mins.

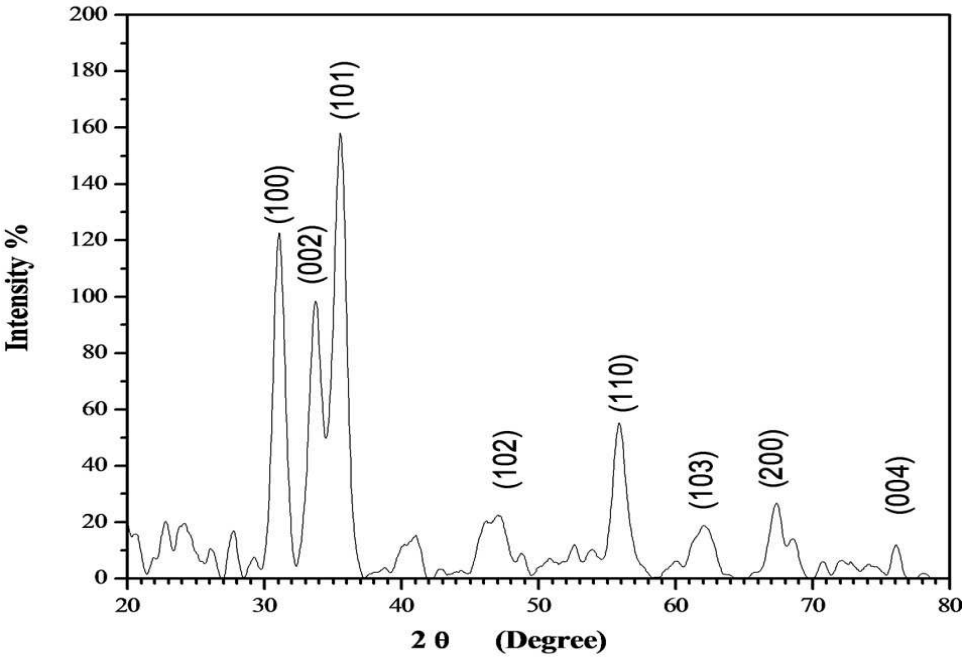

Figure 28 Typical XRD spectrum ZnO thin film.[1]

Lower temperatures where studied by decreasing the substrate temperature every 10 ºC starting from 300 ºC. Table 2 shows the ZnO thin films deposited at 290 ºC.

Table 2. Growth condition and thickness of ZnO thin films at 290 ºC

	Pressure (Torr)	Laser energy (mJ)	Distance (cm)	Time (min)	Thickness (nm)	Ablation rate (nm/min)
20	1.7×10^{-6}	205	3.5	60	36.96	0.62
21	1.5×10^{-5}	220	3.5	60	38.15	0.64
22	2.1×10^{-5}	214	3.5	75	50.52	0.67
23	1.9×10^{-6}	190	3.5	75	--	--
24	2.5×10^{-6}	224	3.5	90	100.17	1.11
25	2.3×10^{-6}	201	3.5	90	--	--

-- Data not acquired.

Similarly as deposition at 300 ºC, a higher laser energy yields a higher ablation rate if you compare sample 24, sample 21 and sample 20. In order to figure out if the lower substrate temperature still can produce the crystalline structure of a ZnO thin film, XRD was used. Figure 29 shows the XRD spectrum of sample 24 which shows there are two orientations of the crystalline structures of ZnO thin film. One orientation is (002) and another one is (103). It is necessary to indicate that two

different orientations are never showing up in any other deposition conditions. The huge peak at degree 70 ° is caused by the substrate silicon wafer. For all the other samples, which were fabricated at 290 ºC, the acquired spectrums have only one peak indicate the orientation (002).

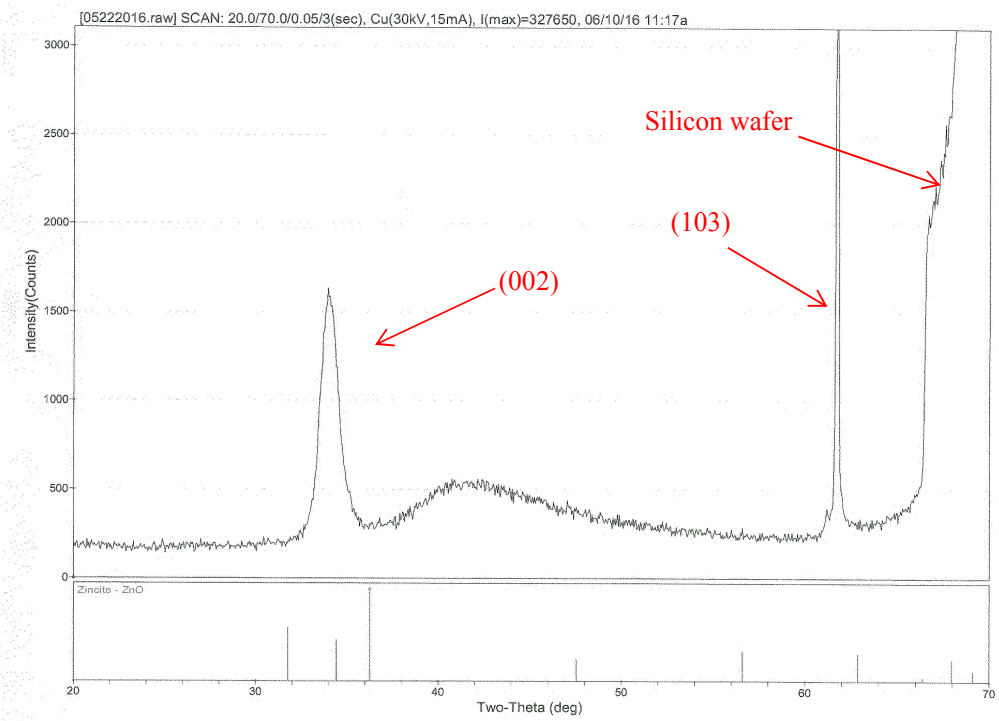

Figure 29 XRD spectrum of sample 24,
2.5×10^{-6} Torr, 290 ºC, 224 mJ and 90 mins.

Table 3 shows the ZnO thin films deposited at 280 ºC.

Table 3. Growth condition and thickness of ZnO thin films at 280 ºC

	Pressure (Torr)	Laser energy (mJ)	Distance (cm)	Time (min)	Thickness (nm)	Ablation rate (nm/min)
26	1.0×10^{-6}	211	3.5	60	53.88	0.90
27	1.2×10^{-5}	221	3.5	60	61.78	1.02
28	1.0×10^{-5}	211	3.5	75	56.89	0.76
29	1.1×10^{-6}	197	3.5	75	54.57	0.73
30	1.9×10^{-6}	226	3.5	90	70.96	0.79
31	1.4×10^{-6}	210	3.5	90	-	-

-- Data not acquired.

Similarly as the deposition at 300 ºC and 290 ºC, the higher laser energy yields a higher ablation rate if you compare sample pairs: sample 27 and sample 26, and sample 28 and sample 29. The data shows that when the deposition time is increasing the ablation rate is dropping. This is might have occurred because the beginning amorphous surface generated all the ejected particles and they were sticking onto the substrate surface. Then when the crystalline structure growth began, the particles landed on the film based on the selections of the crystalline structure. This selections influence the laser ablation rate of grown thin films. XRD has been used to analyze

the samples obtained at 280 ºC. Figure 30 shows the XRD spectrum of sample 24 which shows there is only one orientation of the crystalline structure of the ZnO thin film. Similar spectrums have been acquired by XRD for the other samples that were fabricated at 280 ºC.

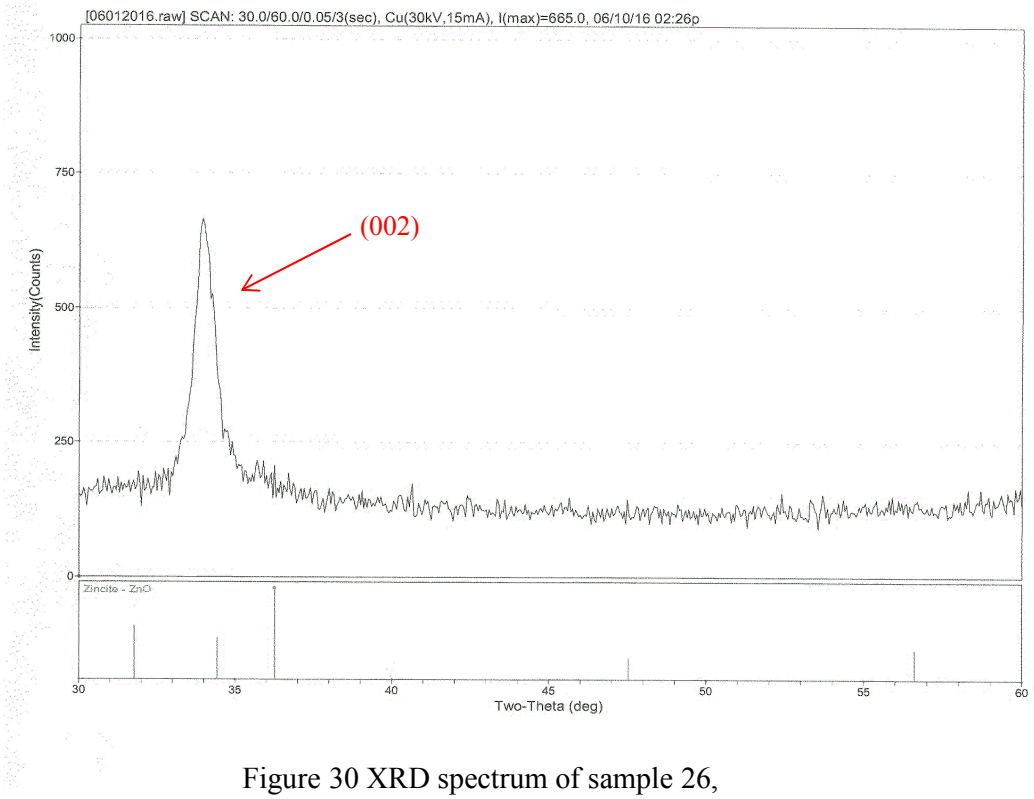

Figure 30 XRD spectrum of sample 26,
1.0×10^{-6} Torr, 280 ºC, 211 mJ and 60 mins.

Table 4 shows the ZnO thin films deposited at 270 ºC.

Table 4. Growth condition and thickness of ZnO thin films at 270 ºC

	Pressure (Torr)	Laser energy (mJ)	Distance (cm)	Time (min)	Thickness (nm)	Ablation rate (nm/min)
32	1.3×10^{-6}	190	3.5	60	55.50	0.93
33	1.6×10^{-6}	227	3.5	60	61.16	1.02
34	1.5×10^{-6}	214	3.5	75	63.42	0.85
35	1.5×10^{-6}	201	3.5	75	--	--
36	1.2×10^{-6}	202	3.5	90	67.84	0.75
37	1.1×10^{-6}	197	3.5	90	66.85	0.74

-- Data not acquired.

Similarly as the deposition at 300 ºC, 290 ºC and 280 ºC, the higher laser energy yields a higher ablation rate for the sample pairs: sample 32 and sample 33, and sample 36 and sample 37. Much like data from table 3, when the deposition time increases the ablation rate drops. XRD was also used to analyze the samples obtained at 270 ºC. Figure 31 shows the XRD spectrum of sample 34 which shows there is still only one orientation of the crystalline structure of the ZnO thin film. And the substrate silicon wafer generates another peak. Similar spectrums have been acquired by XRD

for the other samples that were fabricated at 270 ºC. A substrate temperature of 270 ºC can still yield a crystalline structure of ZnO thin films.

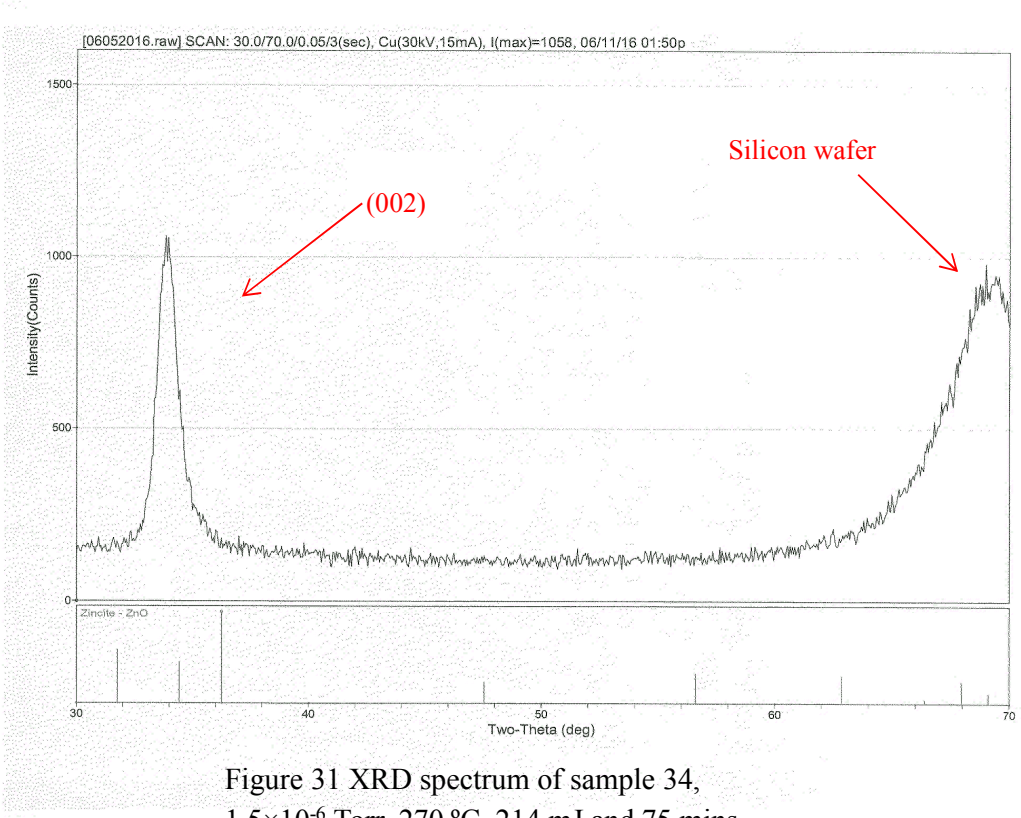

Figure 31 XRD spectrum of sample 34,
1.5×10^{-6} Torr, 270 ºC, 214 mJ and 75 mins.

Table 5 shows the ZnO thin films deposited at 260 ºC.

Table 5. Growth condition and thickness of ZnO thin films at 260 ºC

	Pressure (Torr)	Laser energy (mJ)	Distance (cm)	Time (min)	Thickness (nm)	Ablation rate (nm/min)
38	1.5×10^{-6}	192	3.5	60	43.11	0.72
39	1.6×10^{-5}	221	3.5	60	47.38	0.79
40	1.2×10^{-5}	206	3.5	75	46.31	0.62
41	1.8×10^{-6}	199	3.5	75	45.26	0.60
42	1.3×10^{-6}	200	3.5	90	51.06	0.57
43	1.4×10^{-6}	189	3.5	90	44.34	0.49

Similarly as thin film deposition at 300 ºC, 290 ºC, 280 ºC and 270 ºC, the higher laser energy yields a higher ablation rate when you compare the data from the sample pairs: sample 38 and sample 39, sample 40 and sample 41, and sample 42 and sample 43. Much like the data from table 3 and table 4, when the deposition time increases the ablation rate drops. XRD has also been used to analyze the samples obtained at 260 ºC. Figure 32 shows the XRD spectrum of sample 38. From figure 33, the data from the sample shows there is still only one orientation of the crystalline structure of the ZnO thin film. Compared with previous data, the peak from the spectrum is not as strong as before. This might be because the crystalline structure

developed at this substrate temperature is not as obvious as the crystalline structure developed at higher substrate temperatures. Similar spectrums have been acquired by XRD for the other samples that were fabricated at 260 ºC. Even though the peak is weak at this temperature, it still yields the crystalline structure of ZnO thin films.

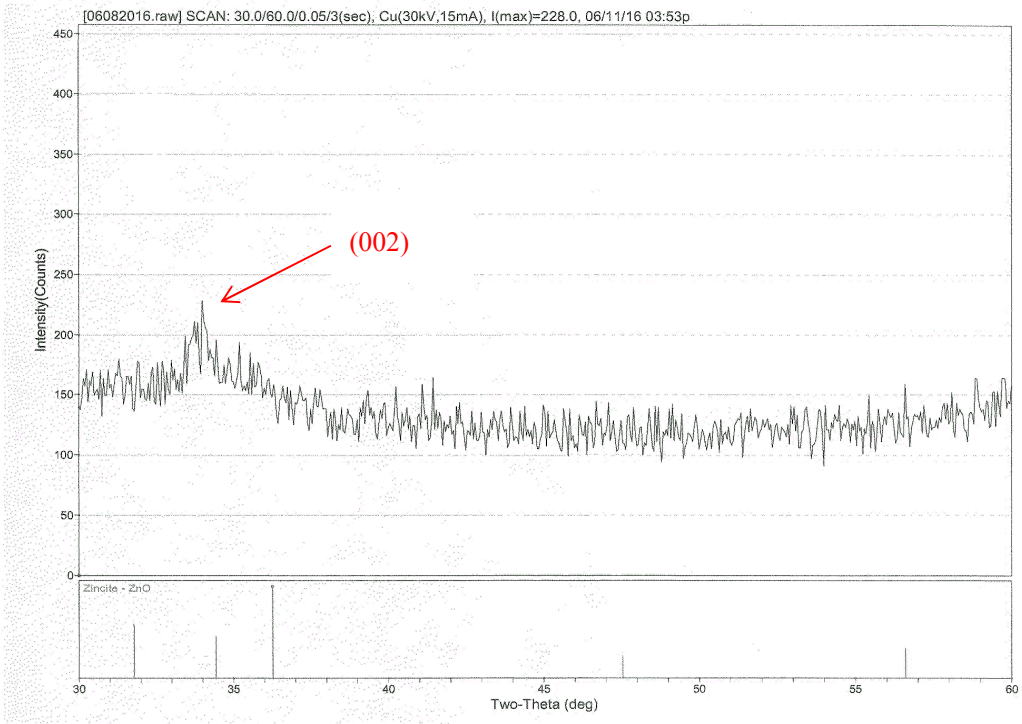

Figure 32 XRD spectrum of sample 38,
1.5×10^{-6} Torr, 260 ºC, 192 mJ and 60 mins.

Table 6 shows the ZnO thin films deposited at 260 ºC.

Table 6. Growth condition and thickness of ZnO thin films at 250 ºC

	Pressure (Torr)	Laser energy (mJ)	Distance (cm)	Time (min)	Thickness (nm)	Ablation rate (nm/min)
44	1.1×10^{-6}	210	3.5	30	13.42	0.45
45	1.3×10^{-6}	207	3.5	45	19.62	0.44
46	8.0×10^{-6}	186	3.5	45	19.62	0.44
47	5.8×10^{-6}	171	3.5	45	13.42	0.30
48	1.5×10^{-6}	206	3.5	75	30.12	0.40
49	4.4×10^{-6}	185	5	30	10.25	0.34
50	5.2×10^{-6}	187	5	45	12.75	0.28
51	4.3×10^{-6}	162	5	75	12.16	0.16

Similarly as the deposition at 300 ºC, 290 ºC, 280 ºC and 270 ºC, the higher laser energy yields a higher ablation rate (From sample 44 to sample 51). Much like the data from previous three tables, when the deposition time increases the ablation rate drops. XRD was also used to analyze the samples obtained at 250 ºC. Figure 33 shows the XRD spectrum of sample 48. From figure 33, the data from the sample shows there is no peak stands for the crystalline structure of the ZnO thin film, but only one peak for the silicon wafer. Compared with previous data, this fabricated ZnO thin film

has only an amorphous surface instead of a crystalline structure. This means the critical substrate temperature of growing crystalline structure ZnO thin films is above 250 ºC and below 260 ºC. For all the other samples from table 6, similar spectrums were acquired by XRD. During the deposition of the thin films, the substrate temperatures were unable to be fixed exactly on a specific temperature. The accuracy varies by 3 ºC, so it can be estimated the critical temperature for fabricating crystalline structure ZnO thin films is 260 ºC.

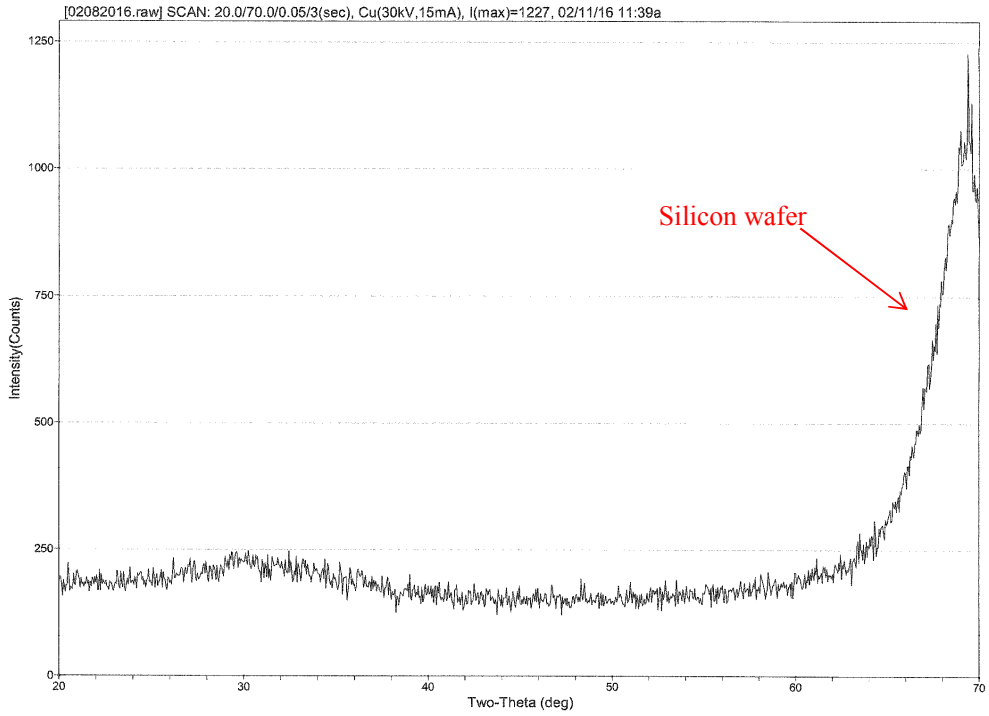

Figure 33 XRD spectrum of sample 48,
1.5×10^{-6} Torr, 250 ºC, 206 mJ and 75 mins.

The band gap energy of the crystalline structure ZnO thin films was determined from the UV-Vis spectroscopy. Since UV-Vis spectroscopy required the sample to be transparent, a glass slide instead of a silicon wafer was used for depositing the ZnO thin films. Two samples were prepared for the measurements: one was deposited for 90 minutes and the other was deposited for 60 minutes with the same remaining conditions (300 ºC, 223mJ, 5Hz, 3.5cm, 1.5×10^{-6} Torr). And both of sample 52 and sample 53 have been tested by XRD in order to make sure both of them have the similar crystalline structure as the previous tables.

Table 7. Growth condition and thickness of ZnO thin films at 300 ºC on glass

	Pressure (Torr)	Laser energy (mJ)	Distance (cm)	Time (min)	Thickness (nm)	Ablation rate (nm/min)
52	1.5×10^{-6}	223	3.5	60	--	--
53	1.5×10^{-6}	223	3.5	90	--	--

-- Data not acquired.

In Figure 34, the red curve represents the absorption spectrum of the thin film that was fabricated by depositing for 90 mins, the blue curve shows the absorption spectrum if the deposition continues for 60 mins, and the black curve shows the absorption of a transparent glass substrate. The linear extrapolation of the absorption

plots in the thin films crosses the abscissa at 379 nm, which corresponds to the energy band gap in the material. The room temperature band gap of the two ZnO thin films, estimated from the absorption spectra, was 3.20 eV. In order to confirm about this calculated band gap energy Tauc equation has been used for calculating band gap energy since this is a more accurate method. Tauc plot (Figure 35) has been drawn based on the data from UV-Vis spectroscopy and calculated by using Tauc equation (2.16) then shows as figure 35. The result of band gap energy from Tauc plot is estimate as 3.12 eV, which is close to the earlier different calculated result 3.20 eV and the reported value of 3.37 eV.[23, 39]

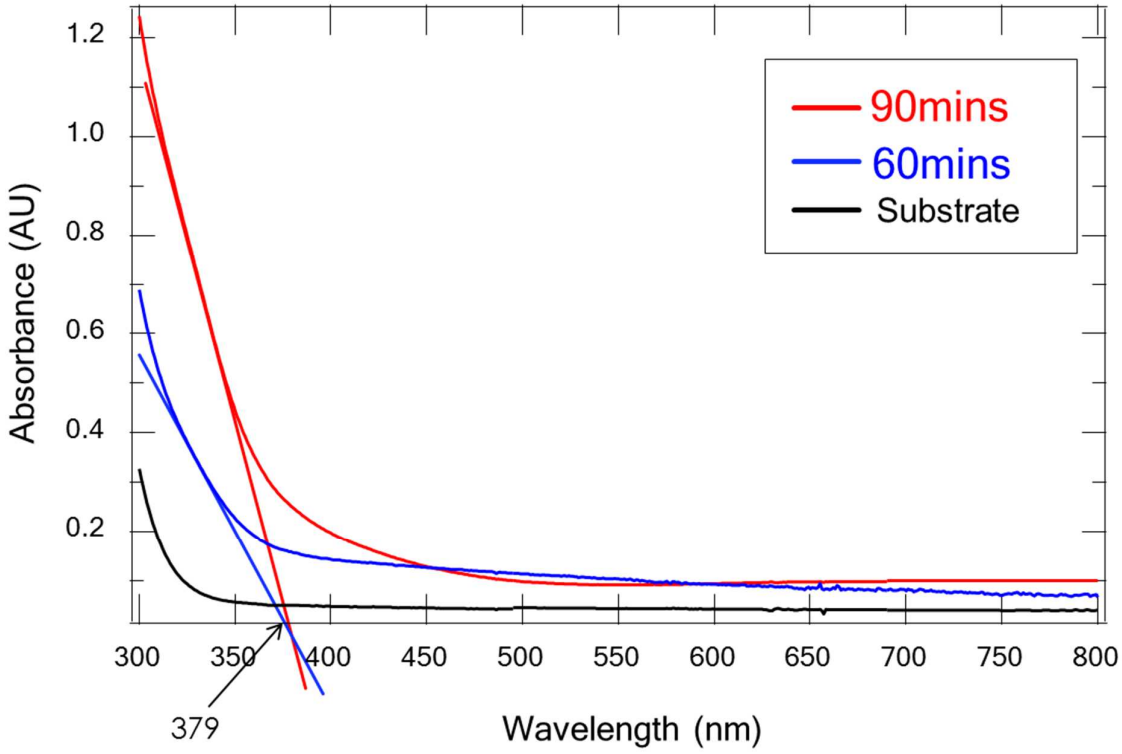

Figure 34 UV-Visible spectrum of ZnO thin film.

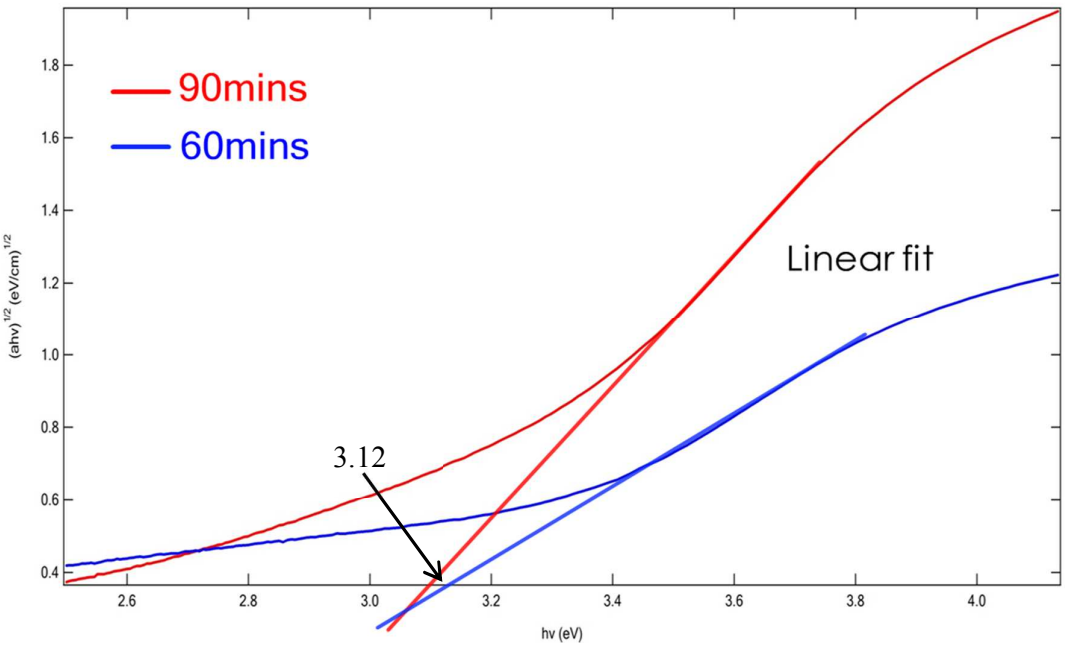

Figure 35 Tauc plot of crystalline structure of ZnO thin film.

4.3 Characterization of SnO_2 thin films

The conditions of the SnO_2 film preparation as well as the deposition time and thickness of the films are listed in following tables:

Table 8. Growth conditions and thickness of SnO_2 thin films at 300 ºC

	Pressure (Torr)	Laser energy (mJ)	Time (min)	Thickness (nm)	Ablation rate (nm/min)
54	2.5×10^{-6}	202	30	43.05	1.44
55	4.6×10^{-6}	219	30	24.58	0.82
56	6.7×10^{-6}	229	45	67.76	1.51
57	3.6×10^{-6}	204	45	44.27	0.98
58	1.0×10^{-5}	229	60	69.26	1.15
59	4.1×10^{-6}	222	60	67.54	1.13
60	9.2×10^{-6}	209	75	107.23	1.43
61	3.4×10^{-6}	231	75	76.45	1.02
62	4.0×10^{-6}	214	90	80.31	0.89
63	8.9×10^{-6}	216	90	146.54	1.63

Table 9. Growth conditions and thickness of SnO_2 thin films at 250 ºC

	Pressure (Torr)	Laser energy (mJ)	Time (min)	Thickness (nm)	Ablation rate (nm/min)
64	9.6×10^{-6}	208	60	38.44	0.64
65	1.1×10^{-5}	216	90	53.55	0.60

For the SnO_2 thin films, it was not easy to find out what the key factor was that effected the thin film growth. For example, sample 54 and sample 55 were both fabricated under the same substrate temperature of 300 ºC. However, sample 55 was grown at laser energy of 219 mJ which was slightly higher than the 202 mJ used during growth of sample 54. The pressure during the growth of sample 55 was twice as high as that for sample 54. Under these conditions, sample 54 was grown at a rate twice as high as sample 55. However, sample 56 and sample 57 were also fabricated under similar laser power and substrate temperature, but the relationship between the chamber pressure and the deposition rate is reversed. So, the two pairs of samples show contradicting results. The pair of samples 60 and 61 were both fabricated under the same substrate temperature of 300 ºC, and the same deposition time of 75 minutes, but the growth pressure for sample 60 was higher. In this case, at a higher pressure, a higher growth rate was observed. Similar results were observed for the pair of samples 56 and 57 and the pair of samples 62 and 63. The above three pairs of

samples indicate that the increase in the chamber pressure is associated with a larger flux of particles in the laser induced plasma. However, sample 58 and sample 59 were grown at the same substrate temperature and very close laser pulse energy, and despite a higher pressure during growth of sample 59, the deposition rate was lower than for sample 58.

The XRD spectra obtained from the SnO_2 thin films fabricated in this experiment show that there were no peaks like the SnO_2 thin films that were grown. This means the films deposited on the silicon substrates kept at 250 ºC or 300 ºC do not crystallize. Unlike the ZnO thin films, the thin films of SnO_2 grown in the specified conditions are amorphous.

SEM was also used to acquire the images of SnO_2 thin films. The film surface and the cross-section of sample 63 is shown in Figure 36. The morphology of the surface suggests that the films were formed by several different shapes of SnO_2 nanoparticles. Some of the particles have a shape of posts and others form clover-like structures. As seen in Figure 36 (a), at the bottom of the film (close to the interface with the substrate) the particles are more compressed than at the surface and they assume a small spherical shape. The nanoparticles at the film surface are larger with a more random shape.

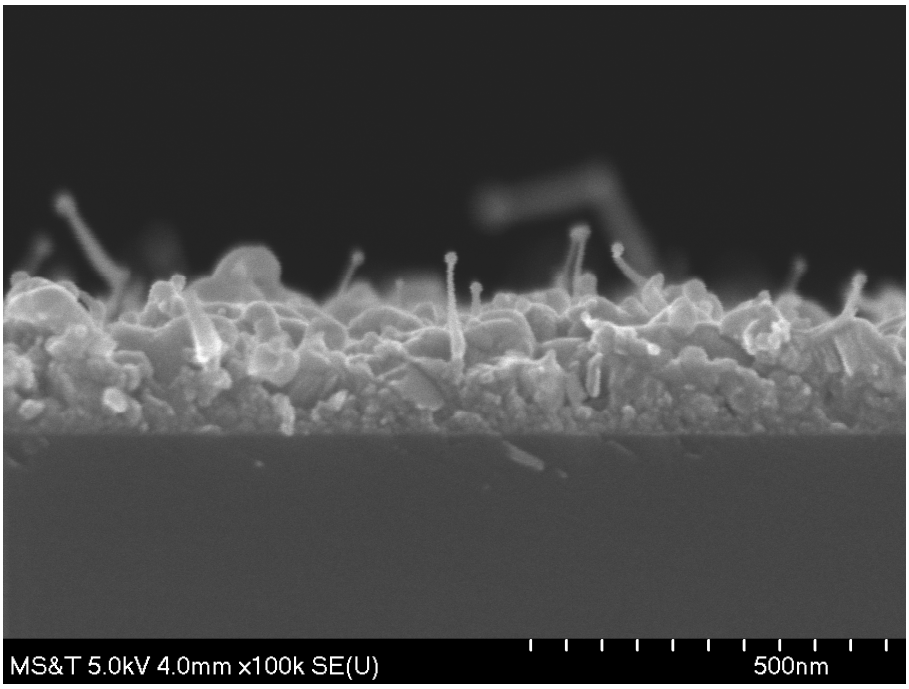

Figure 36 (a)
Side view
Sample 63
8.9×10^{-6} Torr
300 ºC
216 mJ
90 mins

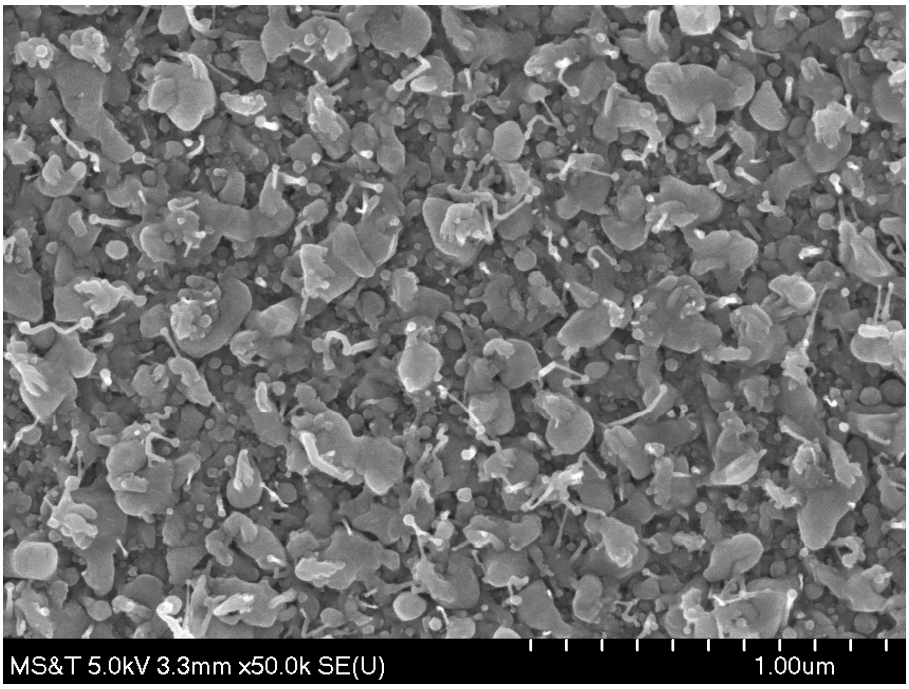

Figure 36 (b)
Top view
Sample 63
8.9×10^{-6} Torr
300 ºC
214 mJ
90 mins

4.4 Annealing SnO_2 thin films

The aim of this research is to predict the crystalline structure of ZnO and SnO_2 thin films. This self-designed pulsed laser deposition system never made SnO_2 thin films successfully, therefore it was necessary to figure out another way to produce the crystalline structure SnO_2 thin films.

Annealing method was a promising technique based on its simple process. Various SnO_2 thin film samples were fabricated under similar conditions to each other. Table 10 shows all these samples have no peaks in the XRD spectrums. In other words, all these SnO_2 thin film samples have an amorphous surface.

Table.10 Growth conditions and thickness of SnO_2 thin films for annealing at 300 ºC

	Material	Pressure (Torr)	Laser energy (mJ)	Distance (cm)	Time (min)	Thickness (nm)	Ablation rate (nm/min)
66	SnO_2	1.1×10^{-5}	221	3.5	60	57.13	0.95
67	SnO_2	8.7×10^{-6}	217	3.5	60	65.24	1.09
68	SnO_2	6.9×10^{-6}	213	3.5	60	37.06	0.62
69	SnO_2	4.7×10^{-6}	202	3.5	60	67.55	1.13
70	SnO_2	3.9×10^{-6}	198	3.5	60	46.42	0.77
71	SnO_2	4.2×10^{-6}	206	3.5	60	59.16	0.99

The equipment that was used for annealing is a digital controlled oven, with a temperature range between room temperature and 1500 ºC. There were 5 different annealing temperatures that were used: 1500 ºC, 700 ºC, 600 ºC, 500 ºC and 400 ºC. The first step in the appealing process is to rapidly heat up the oven to the setting temperature, then hold this temperature for one hour. After this, the oven is turned off and the sample is cooled slowly to room temperature. After annealing the SnO_2 thin films, XRD is used to obtain information about the crystallinity of the sample. Figure 37 shows the XRD spectrum of sample 66 after annealing at 1500 ºC.

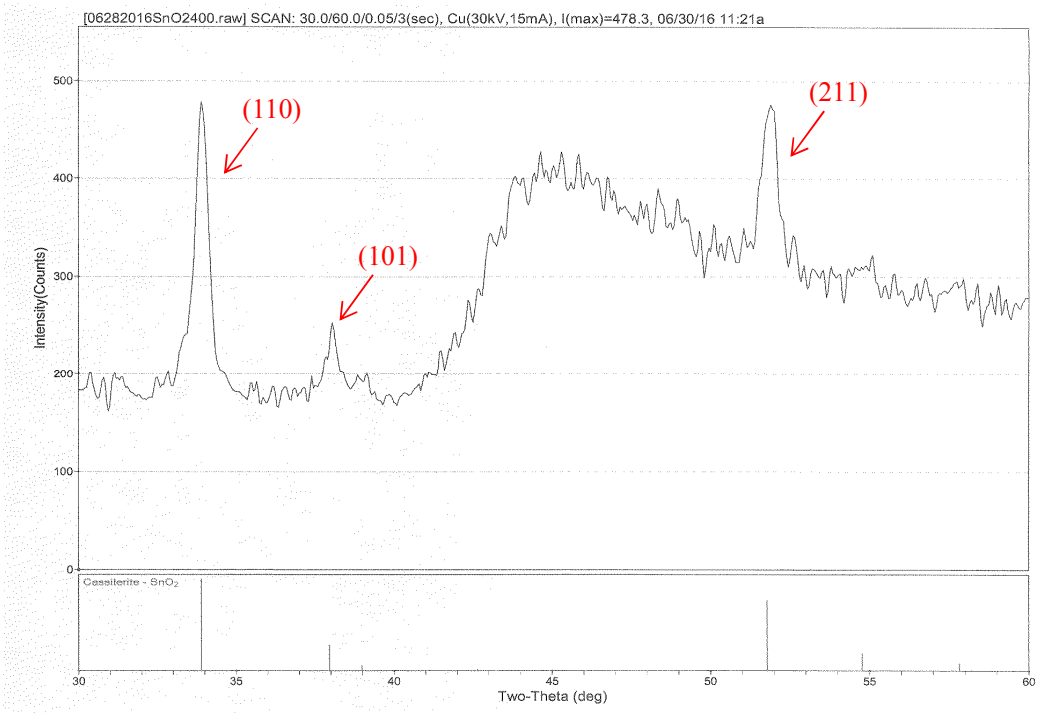

Figure 37 XRD spectrum of sample 66,
1.1×10^{-6} Torr, 300 ºC, 221 mJ and 60 mins.
Annealing temperature 1500 ºC

From the spectrum there are three obvious peaks that show up, which means there are three different orientations (110), (101) and (211). Since there are three orientations shown in the data, it can be concluded that the SnO_2 thin film successfully converts from amorphous surface to crystalline structure.

Figure 38 shows XRD spectrum of sample 67 after annealing at 700 ºC.

In the spectrum there are two small peaks showing up, they are (110) and (211).

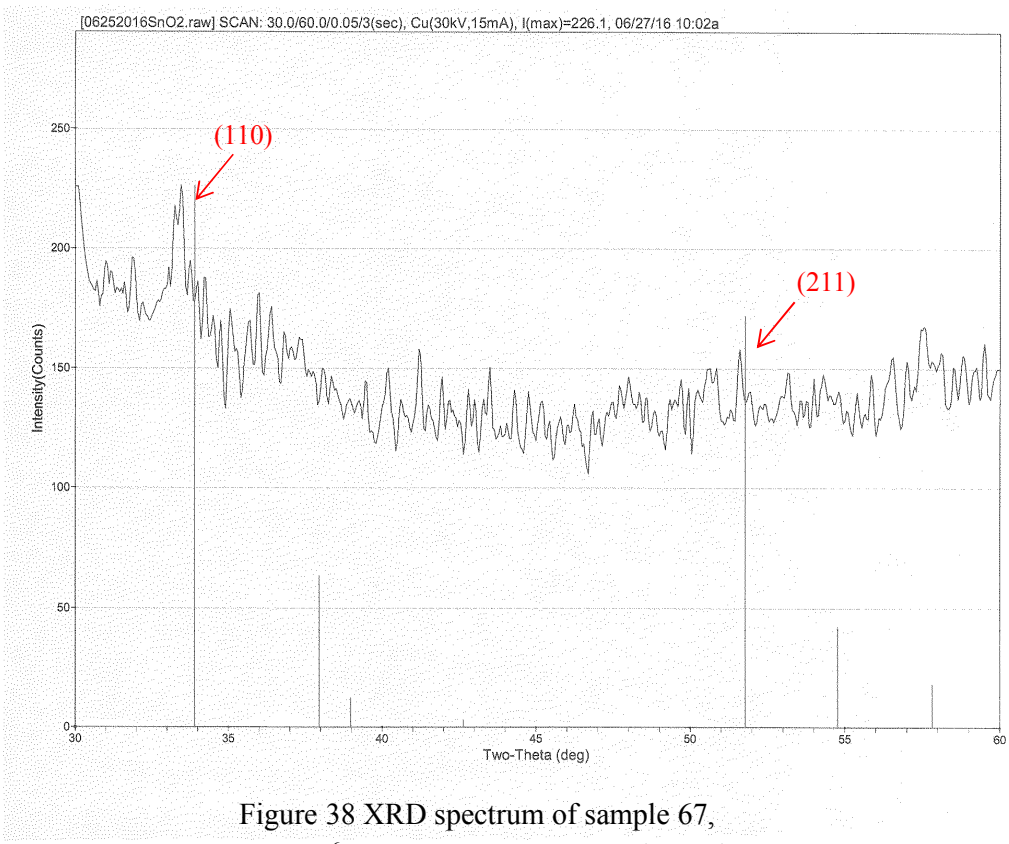

Figure 38 XRD spectrum of sample 67,
8.7×10^{-6} Torr, 300 ºC, 217 mJ and 60 mins.
Annealing temperature 700 ºC

Both of these two orientations are shifted a little bit from the right position. Even though this spectrum is not as good as previous one, we can still see from the data that this SnO_2 thin film still changes from an amorphous surface to crystalline structure.

Figure 39 shows XRD spectrum of sample 68 after annealing at 600 ºC.

Comparing this spectrum with the spectrum in figure 38, we can see the same

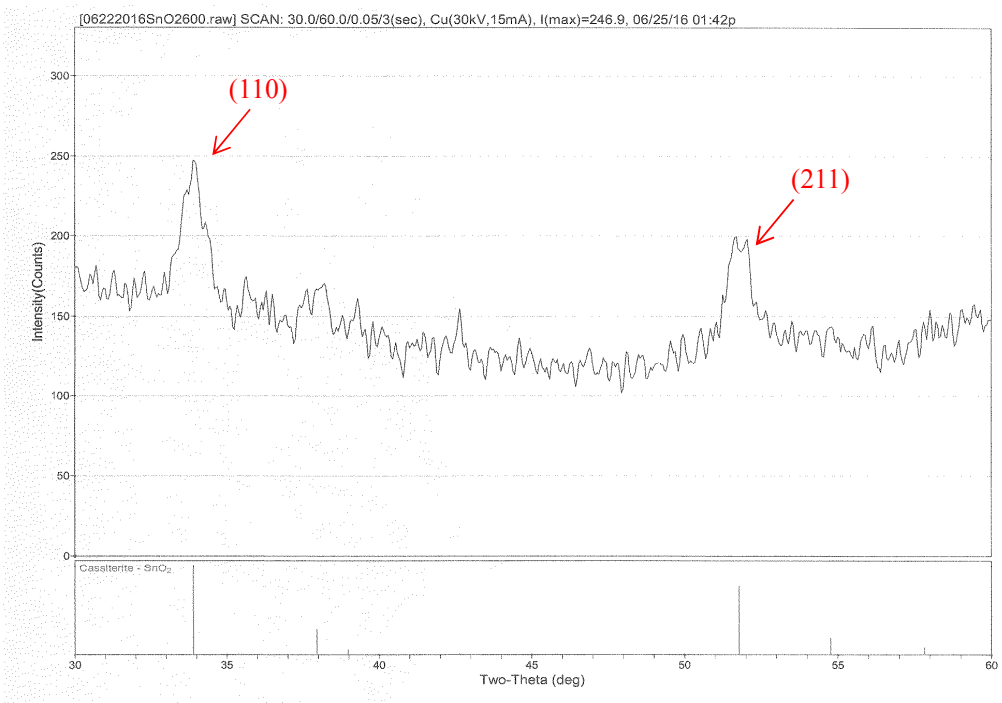

Figure 39 XRD spectrum of sample 68,
6.9×10^{-6} Torr, 300 ºC, 213 mJ and 60 mins.
Annealing temperature 600 ºC

peaks are showing up with better intensity. These peaks are (110) and (211). However, by annealing at 600 ºC we can see from the spectrum both of these two orientations are in the right position. Annealing at 700 ºC or 600 ºC was unable to generate the (101) orientation crystalline structure.

Figure 40 shows XRD spectrum of sample 69 after annealing at 500 ºC.

Similarly as in figure 37, the spectrum has three obvious peaks. There are three

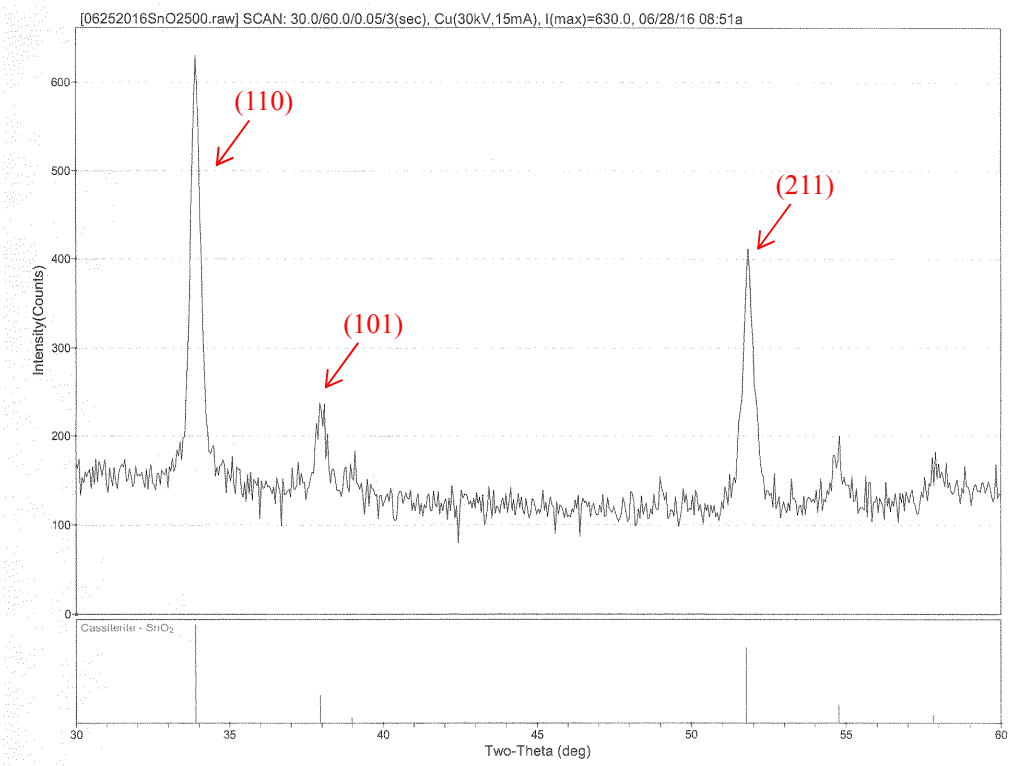

Figure 40 XRD spectrum of sample 69,
4.7×10^{-6} Torr, 300 ºC, 202 mJ and 60 mins.
Annealing temperature 500 ºC

different orientations (110), (101) and (211). By seeing three orientations in the spectra, it can be concluded that the SnO_2 thin film successfully converts from an amorphous surface to crystalline structure. When the annealing temperature is very high (1500ºc) or much lower (500 ºC), three different orientations were converted. However, when the temperature was between 1500 ºC and 500 ºC (such as 700 ºC and 600 ºC) there were only two different orientations of the SnO_2 thin films that were converted from an amorphous surface to a crystalline structure.

So what would happen if the annealing temperature was dropped down to 400 ºC? The answer to this question is given by Figure 41. This is the XRD spectrum of

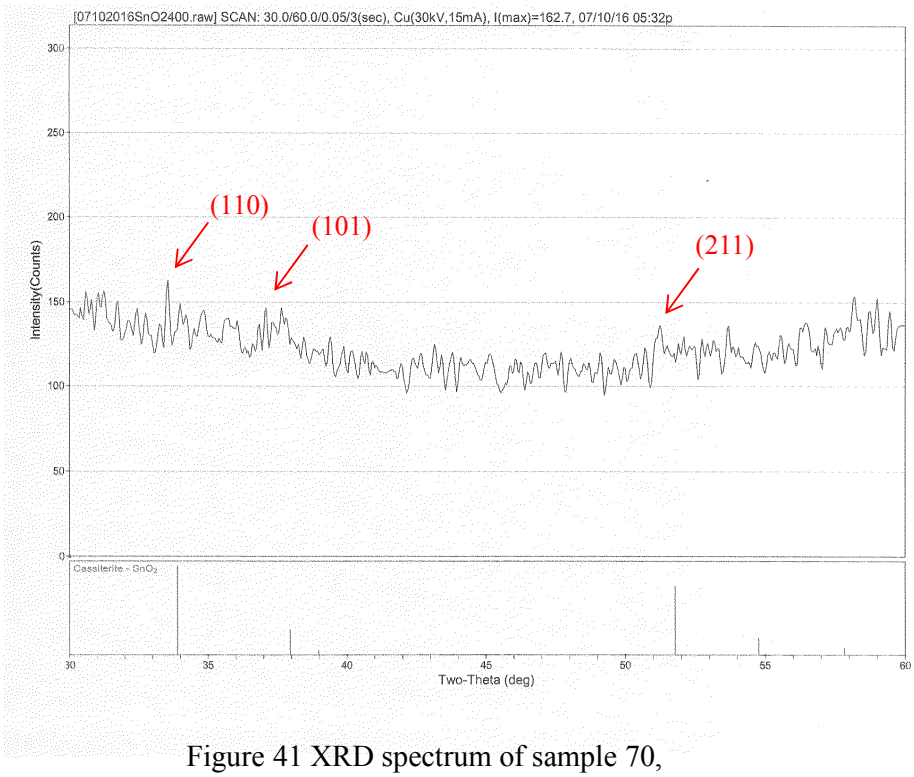

Figure 41 XRD spectrum of sample 70,
3.9×10^{-6} Torr, 300 ºC, 198mJ and 60 mins.
Annealing temperature 400 ºC

sample 70 after annealing at 400 ºC.

We can see from the spectrum there still have some small peaks, but the peak is not obviously as annealing under higher temperature. This means temperature at 400 ºC is close to the critical point which can turn an amorphous into a crystalline structure.

The temperature can vary by 15 ºC even while the oven is held at a specific temperature. The estimated temperature range for converting an amorphous SnO_2 thin film to a crystalline structure is between 415 ºC and 485 ºC. Furthermore, the (101)

orientation can be achieved when the annealing temperature is around 500 ºC or 1500 ºC.

After successful annealing amorphous SnO_2 thin film to crystalline structure. SEM has been used again for observing crystal structure of SnO_2 thin film. The film surface and the cross-section of sample 66 (annealing at 1500 ºC) are shown in Figure 42. The morphology of the surface still has a few posts and spherical structure particles sit on a flat surface. Moreover, this flat surface did not exist in Figure 36 (b). As seen in Figure 42 (a), the film was formed by some elliptical shape of SnO_2 nanoparticles and the size of the nanoparticles is tending to be constant value no matter they located close to the interface with the substrate or on the top of the thin film surface.

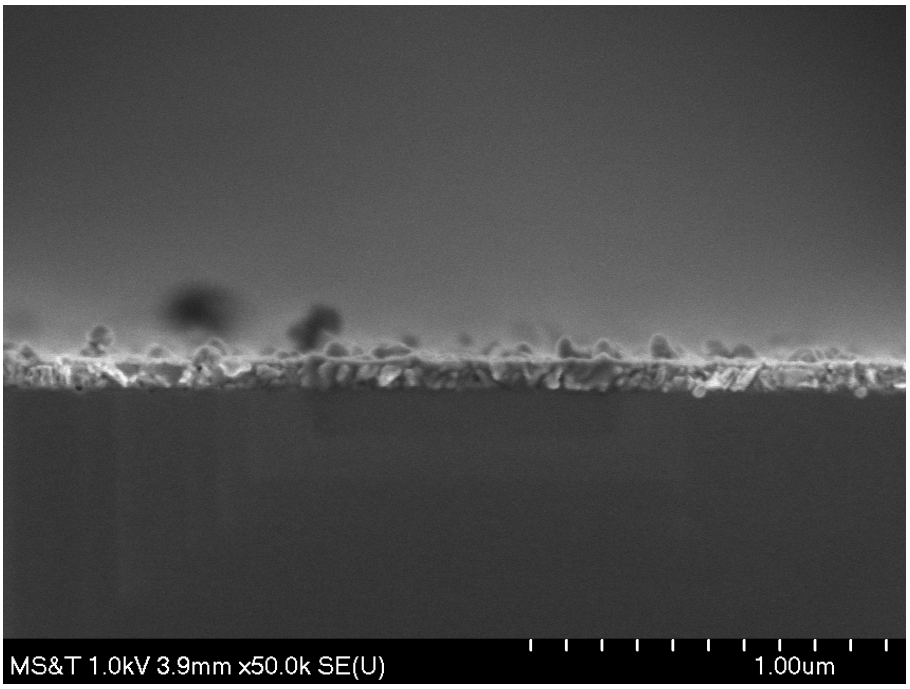

Figure 42 (a) Side view, Sample 66, 1.1×10^{-6} Torr, 300 ºC, 221 mJ 60 mins

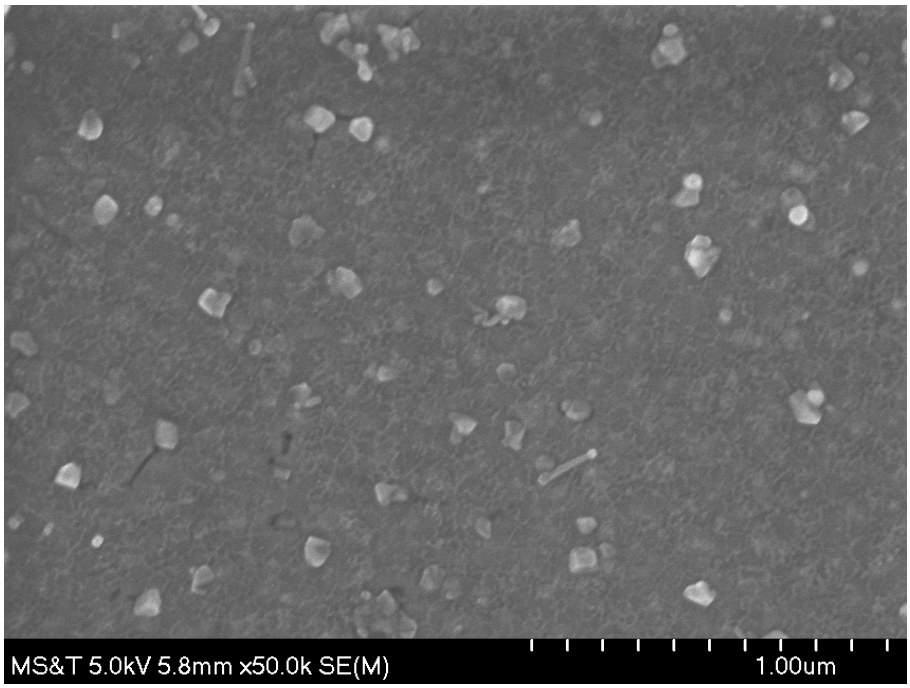

Figure 42 (b) Top view, Sample 66, 1.1×10^{-6} Torr, 300 ºC, 221 mJ 60 mins

4.5 Annealing ZnO thin films

From the previous data we can see that the annealing method works to convert an amorphous SnO_2 thin film to a crystalline structure thin film, but what about an amorphous ZnO thin film? Table 11 shows several ZnO thin film samples have been fabricated under similar conditions at 250 ºC. None of these samples have peaks on the XRD spectrums. In other words, all of these ZnO thin film samples have an amorphous surface.

Table.11 Growth conditions and thickness of ZnO thin films for annealing at 250 ºC

	Material	Pressure (Torr)	Laser energy (mJ)	Distance (cm)	Time (min)	Thickness (nm)	Ablation rate (nm/min)
72	ZnO	2.0×10^{-6}	220	3.5	60	18.16	0.30
73	ZnO	2.1×10^{-6}	216	3.5	60	15.42	0.26
74	ZnO	4.2×10^{-6}	207	3.5	60	17.23	0.29
75	ZnO	3.8×10^{-6}	201	3.5	60	11.26	0.19
76	ZnO	2.7×10^{-6}	198	3.5	60	13.48	0.22

The same method was used for annealing ZnO thing films as was done for SnO_2 thin films, and only 4 different annealing temperatures were used: 1500 ºC, 700 ºC, 600 ºC and 500 ºC. After annealing the ZnO thin films, XRD was still used to obtain information about the crystallinity of the sample. Figure 43 shows XRD spectrum of sample 72 after annealing at 1500 ºC.

From the spectrum we can see there is only one unclear peak which is (002), but this data is strong enough to say that this ZnO thin film was converted to a crystalline structure.

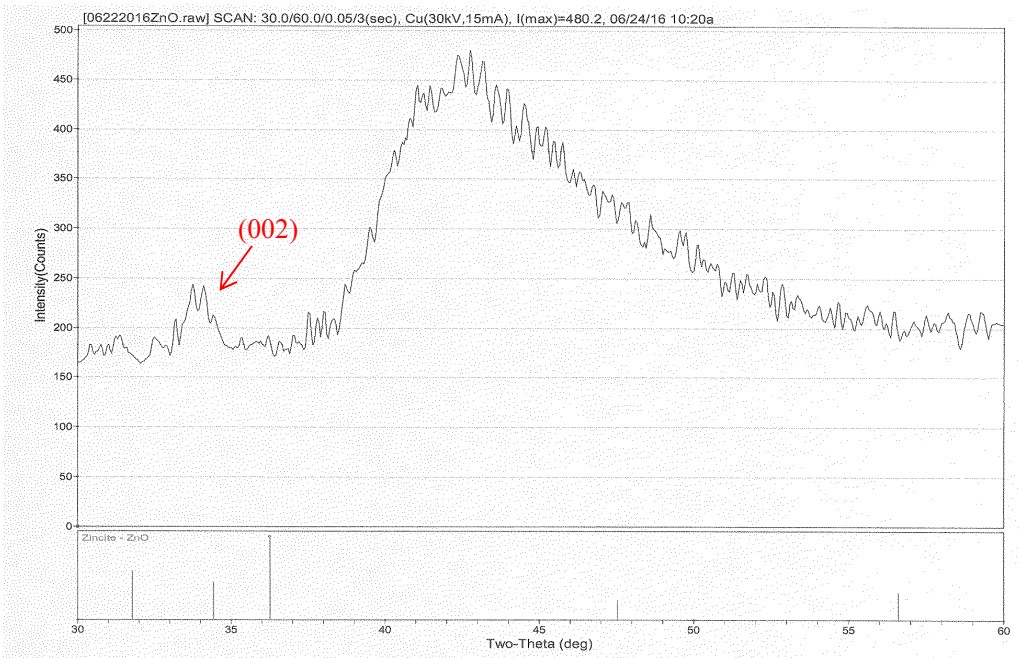

Figure 43 XRD spectrum of sample 72, 2.0×10^{-6} Torr, 250 ºC, 220mJ and 60 mins. Annealing temperature 1500 ºC

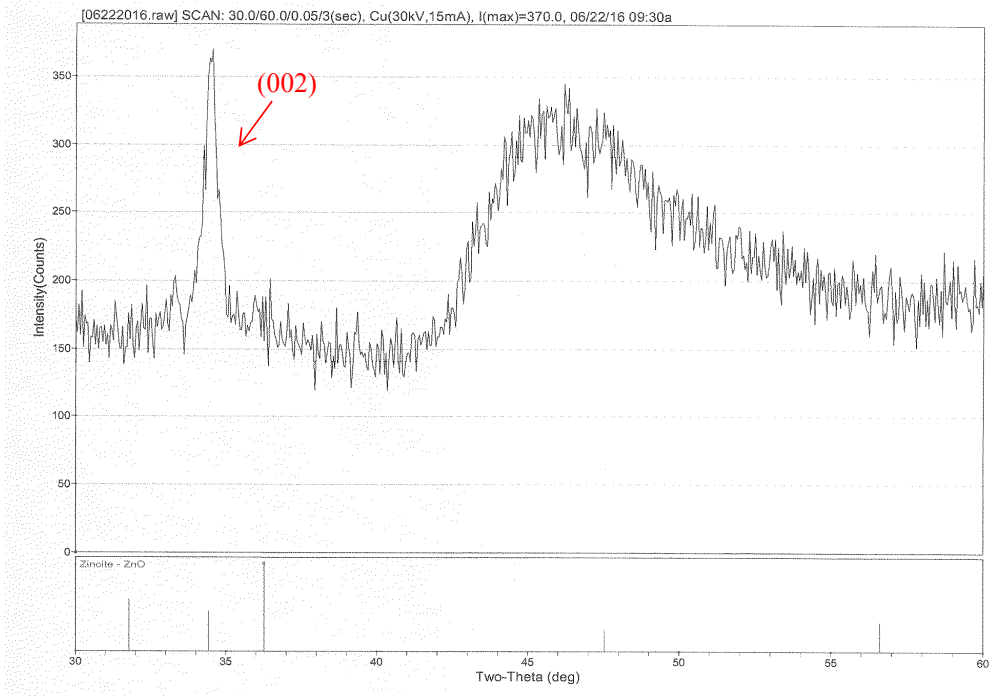

Figure 44 XRD spectrum of sample 73, 2.1×10^{-6} Torr, 250 ºC, 216mJ and 60 mins. Annealing temperature 700 ºC

Figure 44 shows XRD spectrum of sample 73 after annealing at 700 ºC. This

figure is similar but not as same as figure 43. The spectrum has one strong peak which is (002), and from this we can conclude that the ZnO thin film has been converted to crystalline structure. Looking at the data from figure 44, it appears that at a 700 ºC annealing temperature the amorphous ZnO thin film was converted to a better crystalline structure than when the temperature was at 1500 ºC.

Figure 45 shows the XRD spectrum of sample 74 after annealing at 600 ºC.

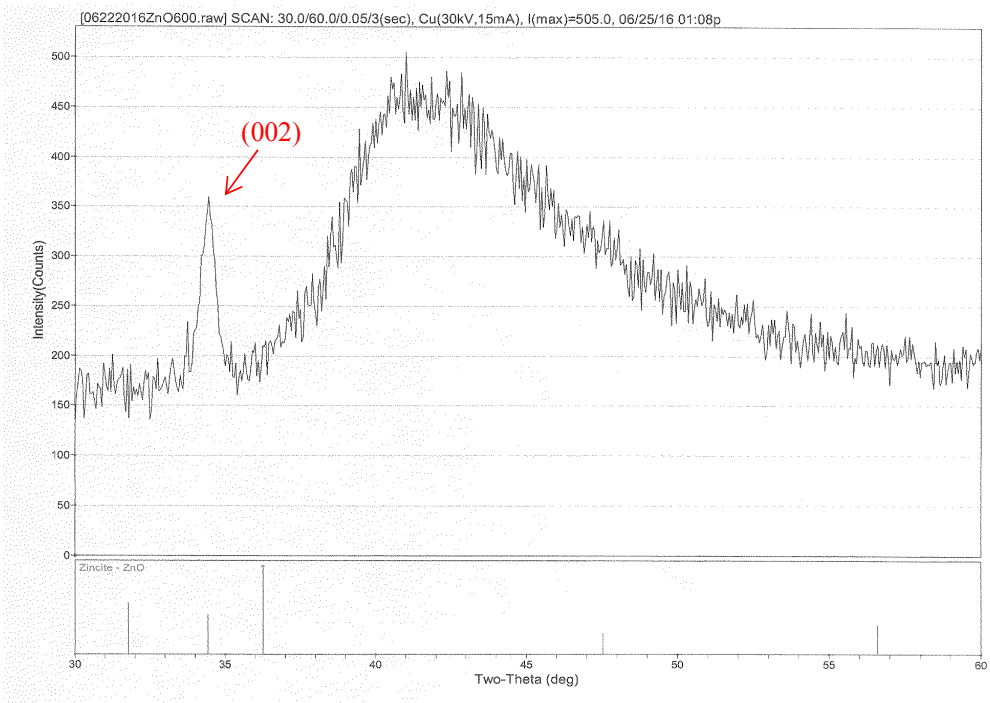

Figure 45 XRD spectrum of sample 74,
4.2×10^{-6} Torr, 250 ºC, 207mJ and 60 mins.
Annealing temperature 600 ºC

This spectrum is similar to that of figure 43, which has only one strong peak (002). This ZnO thin film was also converted to crystalline structure. Annealing at both 600 ºC and 700 ºC produces a great product for amorphous ZnO thin films.

Figure 46 shows XRD spectrum of sample 75 after annealing at 500 ºC.

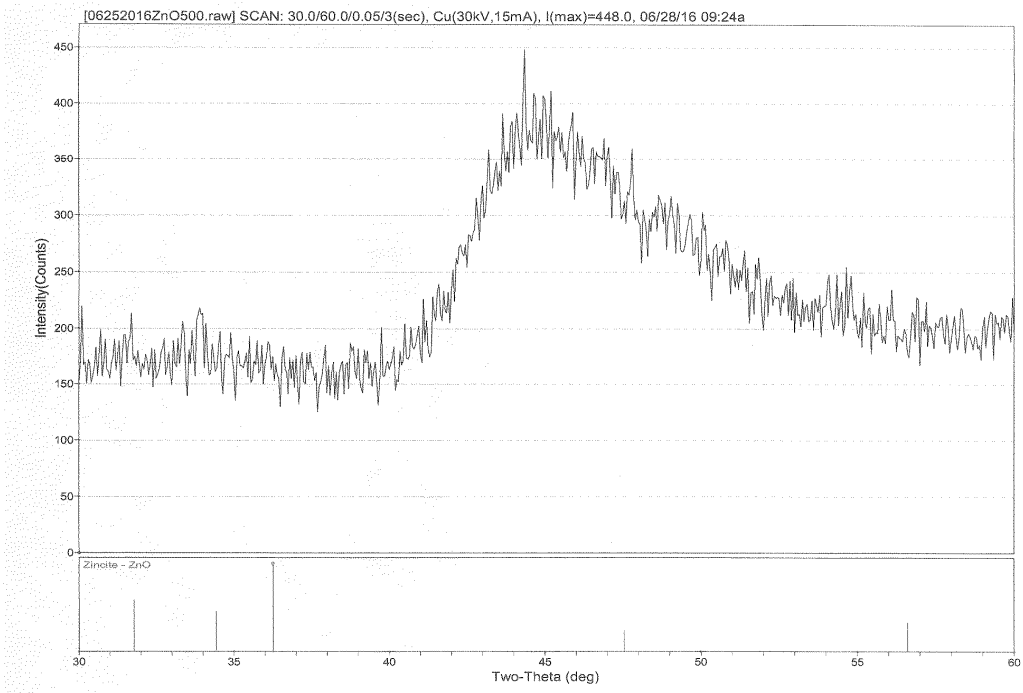

Figure 46 XRD spectrum of sample 75,
3.8×10^{-6} Torr, 250 ºC, 201mJ and 60 mins.
Annealing temperature 500 ºC

From the spectrum we can see there are no peaks, which means the thin film is still an amorphous surface and was not converted into a crystalline structure.

Just like with SnO_2, the temperature can vary 15 ºC even while the oven is held at a specific temperature. The estimated range of temperatures for converting an amorphous ZnO thin film into a crystalline structure is between 515 ºC and 585 ºC. Furthermore, only (002) orientation can be achieved when the annealing temperature higher than 585 ºC.

Same as SnO_2, SEM has been used again for observing crystalline structure of ZnO thin film, which converts from amorphous surface. It is seen that throughout its

volume, the film is uniform with a wave structure surface. The film surface of the sample 73 (annealing at 700 ºC) is shown in Figure 47 (b). Unlike the smooth and featureless surface of Figure 23, this has more particles on the top.

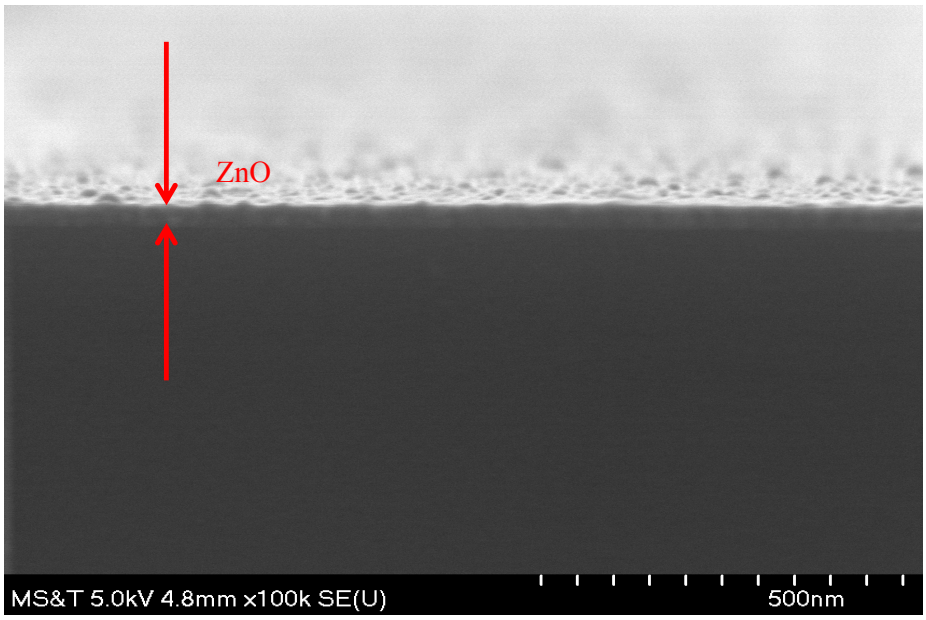

Figure 47 (a) Side view, Sample 73, 2.1×10^{-6} Torr, 250 ºC, 216 mJ 60 mins

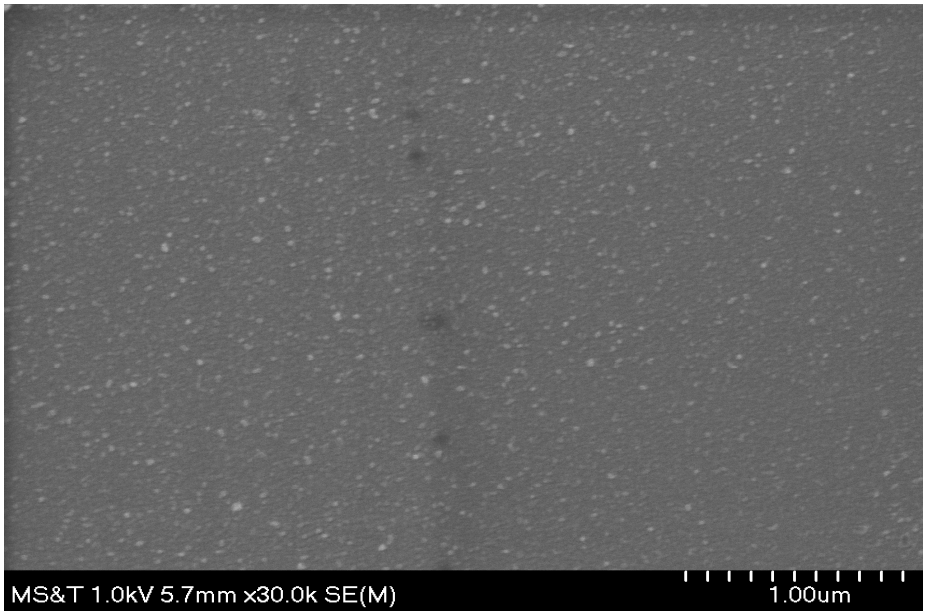

Figure 47 (b) Top view, Sample 73, 2.1×10^{-6} Torr, 250 ºC, 216 mJ 60 mins

4.6 Laser annealing of amorphous thin films

As it was mentioned in chapter 1, there is a new annealing technology called laser annealing. This method was used for both amorphous ZnO and SnO_2 thin films. Sample 71 and sample 76 were analyzed by XRD after they were annealed using a 351 nm XeF excimer laser. For each sample, the laser beam was focused to a diameter of 5mm and then pulsed on the thin film's surface with energy of 7.4 mJ for 20 minutes. Figure 48 and figure 49 show the result of the laser annealing.

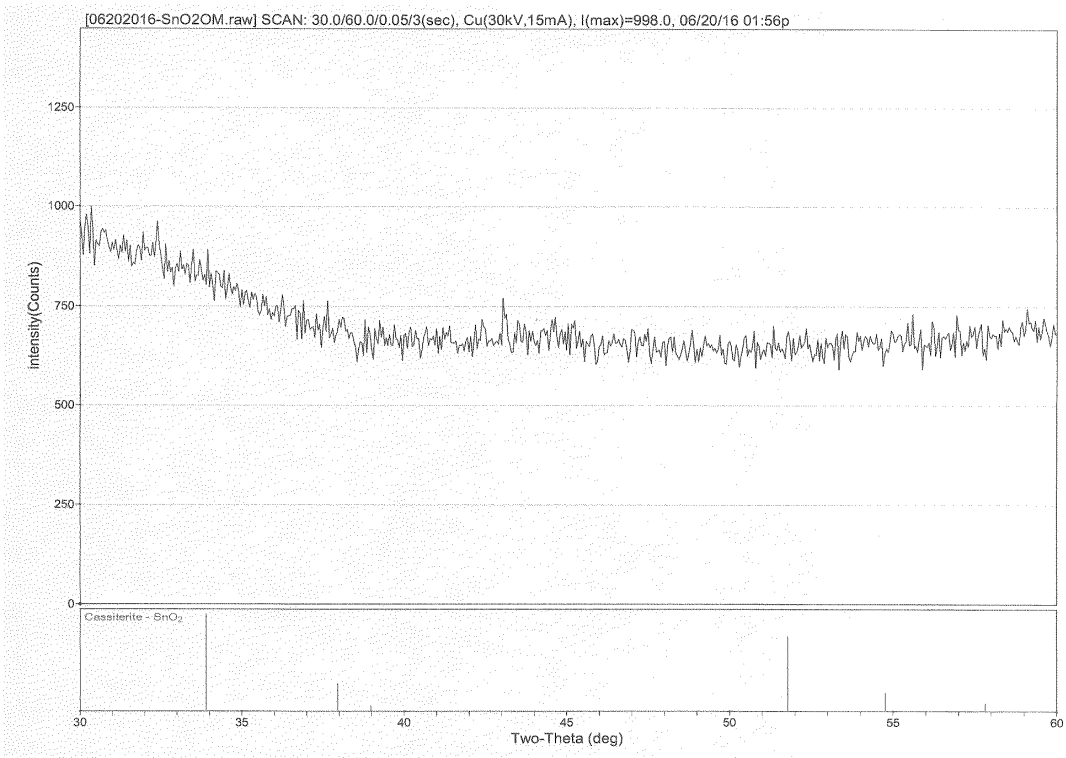

Figure 48 XRD spectrum of sample 71,
4.2×10^{-6} Torr, 300 ºC, 206mJ and 60 mins.
Laser annealing 20 mins.

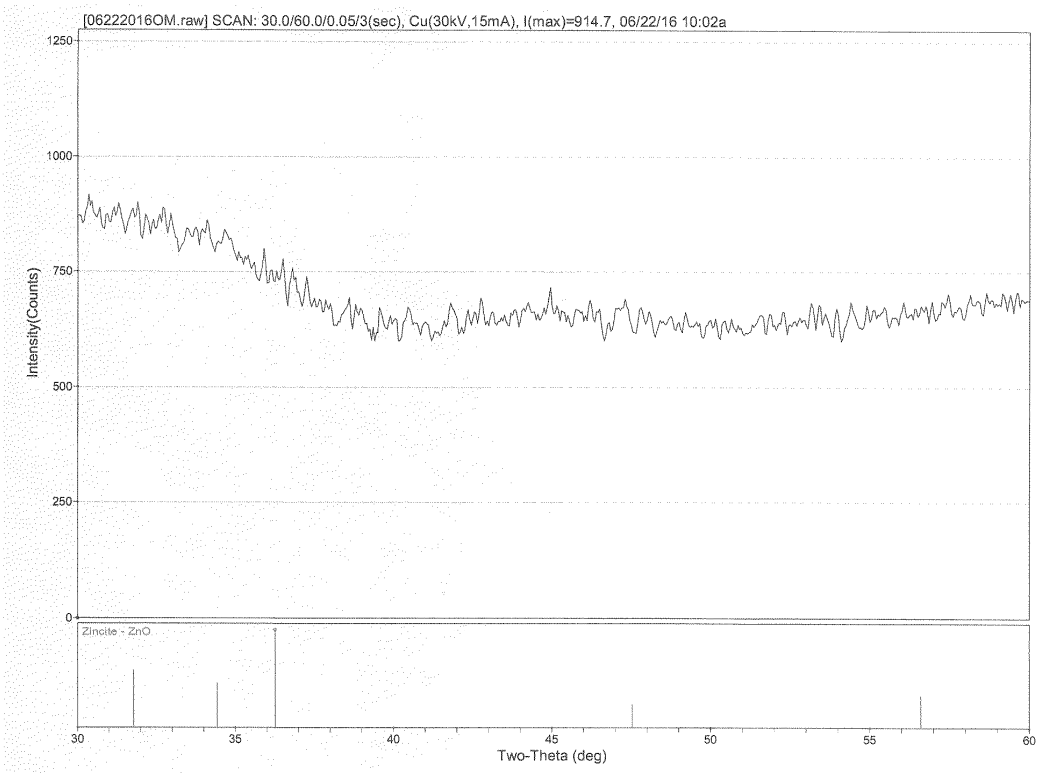

Figure 49 XRD spectrum of sample 76,
2.7×10^{-6} Torr, 250 ºC, 198mJ and 60 mins.
Laser annealing 20 mins.

We can see from figure 48 and figure 49 that there are no peaks, which means both the ZnO and SnO_2 thin films still have amorphous surfaces and they were not converted into crystalline structures. This might be because the laser energy was not high enough or the time was too short for laser annealing.

CHAPTER 5

CONCLUSION

5.1 Conclusion for ZnO thin films

From the results of the experiment the following conclusions can be drawn about pulsed laser deposition of ZnO thin films:

(1) The thickness of the films is proportional to the number of laser pulses.

(2) The substrate temperature during the deposition affects the crystalline structure of the ZnO thin films. 250 ºC is the critical temperature of fabricating crystalline structure ZnO thin films.

(3) The deposition rate rises when the laser pulse energy increases. In figure 50,

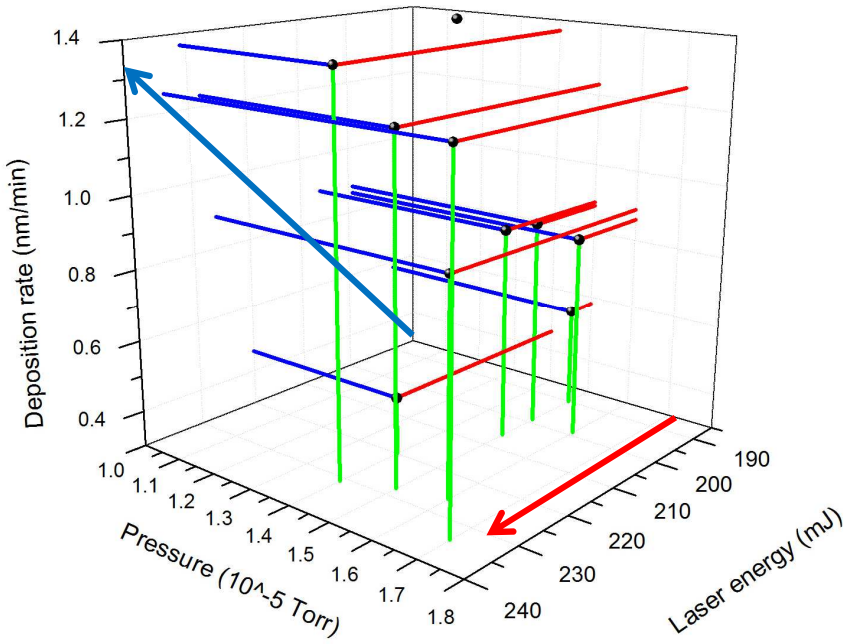

Figure 50 3-D axis based on deposition rate laser energy and pressure.

the red arrow shows the increase of the laser energy and the blue arrow shows the

relationship between the laser energy and the deposition rate (as the laser pulse energy increases the deposition rate increases).

(4) As the deposition time increases the deposition rate decreases.

(5) The ZnO thin films fabricated in this experiment have a featureless surface.

(6) The two different calculation results of band gap energy for (002) crystalline structure ZnO thin films have only 7.4% and 5.0% difference compared with the reported value.

(7) The annealing temperature for amorphous ZnO thin films is between 515 ºC and 585 ºC.

(8) Totally two crystal orientations, which are (002) and (103) were observed through pulsed laser deposition ZnO thin films and annealing amorphous ZnO thin films. However, the orientation (002) was observed in all crystal structure samples but another orientation (103) only been observed when the condition set at pressure is 2.5×10^{-6} Torr, substrate temperature at 290 ºC, laser pulse energy is 224 mJ for 90 mins.

5.2 Conclusion for SnO_2 thin films

From the results of the experiment the following conclusions can be drawn about pulsed laser deposition of SnO_2 thin films:

(1) The thickness of the films is proportional to the number of laser pulses.

(2) It was not possible to obtain crystalline SnO_2 thin films in the specified substrate temperature range (250 ºC - 300 ºC).

(3) Laser pulse energy has little effect on the deposition rate.

(4) The size of the SnO_2 plasma flux is strongly correlated to the chamber pressure during the film growth. In figure 51, the green arrow shows the pressure

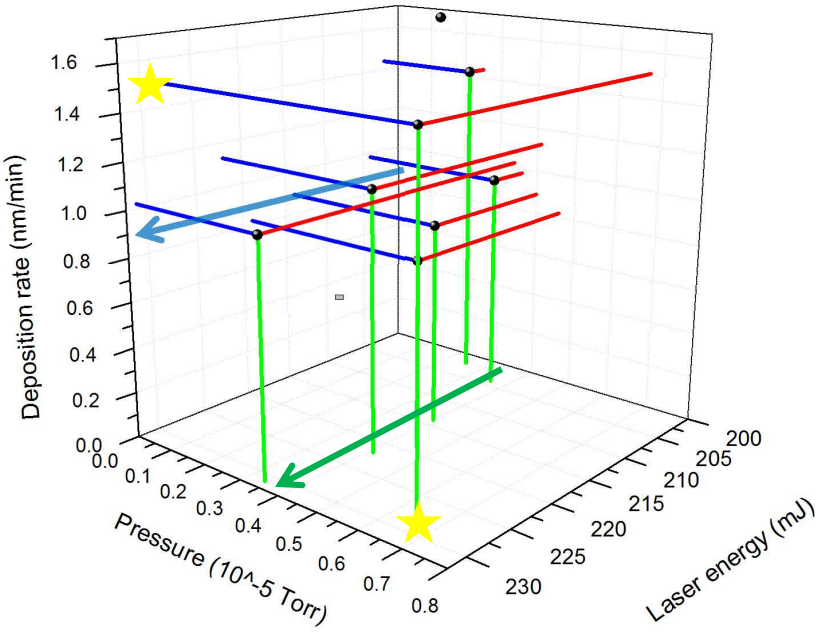

Figure 51 3-D axis based on deposition rate laser energy and pressure.

level of each deposition and blue arrow shows the deposition rate when the pressure is similar. The two yellow stars show that when a difference occurs in the pressure a difference occurs in the deposition rate as well.

(5) The annealing temperature for amorphous SnO_2 thin films is between 415 ºC and 485 ºC.

(6) Three crystal orientations, which are (110), (101) and (211) have been observed through annealing amorphous SnO_2 thin films. The (101) orientation was only achieved when the annealing temperature was at 500 ºC or 1500 ºC.

BIBLIOGRAPHY

1. S. Yamny and M. Rafea, Journal of Modern Physics **Vol. 3**, 1060-1069 (2012).
2. A. Yourdkhani, D. Caruntu, A. K. Perez and G. Caruntu, Journal of Physical Chemistry C **118** (4), 1774-1782 (2014).
3. M. Mallak, M. Bockmeyer and P. Löbmann, Thin Solid Films **515** (20–21), 8072-8077 (2007).
4. P. Hosseini, C. D. Wright and H. Bhaskaran, Nature **511**, 206-211 (2014).
5. C. Jiang, S. Markutsya, Y. Pikus and V. V. Tsukruk, Nature Materials **3**, 721-728 (2004).
6. J. Kao, K. Thorkelsson, P. Bai, Z. Zhang, C. Sun and T. Xu, Nature Communications **5**, 4053 (2014).
7. O. V. Molodtsova, I. M. Aristova, S. V. Babenkov, O. V. Vilkov and V. Y. Aristov, Journal of Applied Physics **115**, 164310 (2014).
8. *Pulsed Laser Deposition of Thin Films*. (Wiley-Interscience, 4/10/2007).
9. H. E. Ives, The Astrophysical Journal **60**, 209 (1924).
10. J.-H. Lee, K.-H. Ko and B.-O. Park, Journal of Crystal Growth **247** (1–2), 119-125 (2003).
11. S. Tsunekawa, Y. Homma, H. Morisaki, S. Okudaira and K. Mukai, (Google Patents, 1986).
12. N. Oleynik, M. Adam, A. Krtschil, J. Bläsing, A. Dadgar, F. Bertram, D. Forster, A. Diez, A. Greiling, M. Seip, J. Christen and A. Krost, Journal of Crystal Growth **248**, 14-19 (2003).
13. Y. J. Choi, K. M. Kang, H. S. Lee and H. H. Park, Journal of Materials Chemistry C **3** (32), 8336-8343 (2015).

14. O. A. Fouad, A. A. Ismail, Z. I. Zaki and R. M. Mohamed, Applied Catalysis B: Environmental **62** (1–2), 144-149 (2006).
15. A. Y. Cho and J. R. Arthur, Progress in Solid State Chemistry **10**, 157-191 (1975).
16. G. Wollenek, G. Laufer, R. Fasol, P. Zilla and E. Wolner, Thoracic and Cardiovascular Surgeon **34** (1), 63-65 (1986).
17. C. Z. Cai, T. T. Xiao, J. L. Tang and S. J. Huang, Physica C: Superconductivity **493**, 100-103 (2013).
18. A. T. Sellinger, A. H. Martin and J. M. Fitz-Gerald, Thin Solid Films **516** (18), 6033-6040 (2008).
19. V. Komenda, V. Myslík, M. Vrňata, F. Vysloužil, P. Fitl, R. Fryček and M. Jelínek, Sensors and Actuators B: Chemical **119** (1), 239-244 (2006).
20. R. Nozaki, S. Nakayama and M. Senna, Thin Solid Films **542**, 214-218 (2013).
21. S. Nakayama, S. Nagare and M. Senna, Thin Solid Films **515** (4), 2582-2586 (2006).
22. F. M. Miroiu, G. Socol, A. Visan, N. Stefan, D. Craciun, V. Craciun, G. Dorcioman, I. N. Mihailescu, L. E. Sima, S. M. Petrescu, A. Andronie, I. Stamatin, S. Moga and C. Ducu, Materials Science and Engineering: B **169** (1–3), 151-158 (2010).
23. B. J. Jin, S. Im and S. Y. Lee, Thin Solid Films **366** (1–2), 107-110 (2000).
24. G. W. Yang, Progress in Materials Science **52** (4), 648-698 (2007).
25. A. V. Simakin, V. V. Voronov and G. A. Shafeev, Physics of Wave Phenomena **15** (4), 218-240 (2007).
26. S. E. Black, *Laser ablation : effects and applications*. (Nova Science Publishers, Hauppauge, N.Y., 2011).
27. T. E. Itina, The Journal of Physical Chemistry C **115** (12), 5044-5048 (2010).

28. P. P. Patil, D. M. Phase, S. A. Kulkarni, S. V. Ghaisas, S. K. Kulkarni, S. M. Kanetkar, S. B. Ogale and V. G. Bhide, Physical Review Letters **58** (3), 238-241 (1987).
29. X. Xu, Applied Surface Science **197-198**, 61-66 (2002).
30. R. K. Singh and J. Narayan, Physical Review B **41** (13), 8843-8859 (1990).
31. J. C. Oliveira, A. Cavaleiro and M. T. Vieira, in *Key Engineering Materials* (2002), Vol. 230-232, pp. 114-117.
32. J. W. Parks, T. A. Wall, H. Cai, A. R. Hawkins and H. Schmidt, IEEE Journal on Selected Topics in Quantum Electronics **22** (6) (2016).
33. Z. Wan, S. Huang, M. A. Green and G. Conibeer, presented at the Conference Record of the IEEE Photovoltaic Specialists Conference, 2010 (unpublished).
34. S. Baco, A. Chik and F. Md Yassin, Journal of Science and Technology **4** (1) (2012).
35. C. Goyes, M. Ferrari, C. Armellini, A. Chiasera, Y. Jestin, G. C. Righini, F. Fonthal and E. Solarte, Optical Materials **31** (9), 1310-1314 (2009).
36. N. Misra, L. Xu, M. S. Rogers, S. H. Ko and C. P. Grigoropoulos, Physica Status Solidi (C) Current Topics in Solid State Physics **5** (10), 3264-3270 (2008).
37. T. H. Kim, S. H. Nam, H. S. Park, J. K. Song and S. M. Park, Applied Surface Science **253** (19), 8054-8058 (2007).
38. A. B. Djurišić and Y. H. Leung, Small **2** (8-9), 944-961 (2006).
39. N. Kamarulzaman, M. F. Kasim and R. Rusdi, Nanoscale Research Letters **10**, 346 (2015).
40. Z. Chen, D. Pan, Z. Li, Z. Jiao, M. Wu, C.-H. Shek, C. M. L. Wu and J. K. L. Lai, Chemical reviews **114** (15), 7442-7486 (2014).

41. S. S. Pan, S. F. Yu, Y. X. Zhang, Y. Y. Luo, S. Wang, J. M. Xu and G. H. Li, Journal of Applied Physics **113** (14) (2013).
42. M. Kumar, A. K. Gupta and D. Kumar, Ceramics International (2015).
43. N. G. Basov, V. A. Danilychev, Y. U. M. Popov and D. D. Khodkevich, JETP Lett **12** (10), 329-331 (1970).
44. Peter W. Milonni and J. H. Eberly, *LASERS*, 1 ed. (Wiley, John & Sons, Incorporated, November, 1988).
45. P. Liu, C. X. Wang, X. Y. Chen and G. W. Yang, Journal of Physical Chemistry C **112** (35), 13450-13456 (2008).
46. C. R. Munnerlyn, S. J. Koons and J. Marshall, Journal of Cataract and Refractive Surgery **14** (1), 46-52 (1988).
47. I. G. Pallikaris and D. S. Siganos, Journal of Refractive and Corneal Surgery **10** (5), 498-510 (1994).
48. J. R. Lankard Sr and G. Wolbold, Applied Physics A Solids and Surfaces **54** (4), 355-359 (1992).
49. D. E. N. Joseph Goldstein, D C. Joy, C E. Lyman, P Echlin, E LIfshin, L Sawyer, and J R. Michael., *Scanning Electron Microscopy and X-ray Microanalysis*, (3 ed) ed. (Springer, 2003).
50. C. G. Jones, in *Methods in Molecular Biology* (2012), Vol. 915, pp. 1-20.
51. R. Schneider, in *Surface and Thin Film Analysis* (Wiley-VCH Verlag GmbH & Co. KGaA, 2011), pp. 293-310.
52. R. Castaing, *Application des sondes électroniques à une méthode d'analyse ponctuelle chimique et cristallographique*. (Office National d'études et de recherches aéronautiques, Chatillon-sous-Bagneux, 1952).
53. W. E. J. Neal, Surface Technology **6** (2), 81-110 (1977).

54. N. M. Bashara and R. M. A. Azzam, J Vac Sci Technol **12** (4), 887-890 (1975).
55. P. Paduschek, M. Tamme and T. D. Hankey, presented at the Proceedings of SPIE - The International Society for Optical Engineering, 1995 (unpublished).
56. J. A. Harrington, B. L. Bobbs, M. Braunstein, R. K. Kim, R. Stearns and R. Braunstein, Applied Optics **17** (10), 1541-1546 (1978).
57. D. L. Allara, presented at the ACS Symposium Series, 1982 (unpublished).
58. T. L. Chester and J. D. Winefordner, Analytical Chemistry **49** (1), 119-123 (1977).
59. L. A. Hanlan, H. Huber, E. P. Kündig, B. R. McGarvey and G. A. Ozin, Journal of the American Chemical Society **97** (24), 7054-7068 (1975).
60. N. S. Gingrich, Physical Review **59** (3), 290-292 (1941).
61. M. L. Huggins, Journal of Chemical Education **22** (7), 364 (1945).
62. J. L. Koenig, Chemische Technik **2** (4), 226-231 (1972).
63. D. V. George, in *Principles of Quantum Chemistry* (Pergamon, 1972), pp. 1-7.
64. D. V. George, in *Principles of Quantum Chemistry* (Pergamon, 1972), pp. 8-21.
65. N. M. Bulgakova and A. V. Bulgakov, Applied Physics A **73** (2), 199-208 (2001).
66. R. Clausius, Mathematische Annalen **4** (2), 231-242 (1871).
67. P. J. F. Gary L. Miessler, Donald A. Tarr,, *Inorganic Chemistry*. (Prentice Hall, 2014).
68. A. Dumbrava, G. Prodan, A. Georgescu and F. Moscalu, Bulletin of Materials Science **38** (1), 65-72 (2015).
69. H. Y. Fan, Reports on Progress in Physics **19** (1), 107-155 (1956).
70. R. K. Willardson, Journal of Applied Physics **30** (8), 1158-1165 (1959).
71. J. Tauc and A. Menth, Journal of Non-Crystalline Solids **8–10**, 569-585 (1972).

72. Y. Li, O. R. Musaev, J. M. Wrobel and M. B. Kruger, Journal of Laser Applications **28** (2) (2016).
73. S. Zoppel, H. Huber and G. A. Reider, Applied Physics A **89** (1), 161-163 (2007).
74. T. C. Damen, S. P. S. Porto and B. Tell, Physical Review **142** (2), 570-574 (1966).
75. X. T. Zhang, Y. C. Liu, Z. Z. Zhi, J. Y. Zhang, Y. M. Lu, D. Z. Shen, W. Xu, G. Z. Zhong, X. W. Fan and X. G. Kong, Journal of Physics D: Applied Physics **34** (24), 3430-3433 (2001).
76. V. Craciun, J. Elders, J. G. E. Gardeniers and I. W. Boyd, Applied physics letters **65** (23), 2963-2965 (1994).

VITA

Yilu Li was born on May 12th, 1988, in Nanjing, Jiangsu Province of P.R.China. In 2010, he graduated from Changchun University of Science and Technology and received a Bachelor's degree of Science. After a short period of working, in August 2011, he moved to United States for his higher education. In 2013, he received his Master's degree in physics at the University of Missouri-Kansas City. He is currently pursuing his Doctorate degree in physics at University of Missouri-Kansas City.

He has worked as a Graduate Teaching Assistant in the Physics Department since January of 2012. He joined Professor Kruger's Condensed Matter Physics Group in June of 2012 and started his physics research career. During his time doing research under Prof. Kruger, he worked with the Post-Doctoral Researcher Omar Musaev doing a project related to laser ablation. After he completed his Master's program he joined Professor Wrobel's group and worked on a project about pulsed laser deposition. In September of 2013, he presented a poster titled "Laser ablation of Ge in liquid in electric field" at 57th Midwest Solid State Conference held by the University of Kansas in Lawrence, KS. In October of 2015, he did an oral presentation titled "Properties of zinc oxide thin films grown on silicon wafers by pulsed laser deposition" at AVS 62nd international symposium & exhibition in San Jose, CA, and at the 2015 Shanghai thin film conference in Shanghai, China. In April of 2016, he did an oral presentation titled "Laser Ablation in Liquids of Germanium in Externally Applied

Electric Fields" at the International High Power Laser Ablation and Directed Energy conference in Santa Fe, New Mexico.